Theoretical study on x-ray spectra from dense plasmas

(高密度プラズマからのX線スペクトルに関する理論的研究)

Takeshi NISHIKAWA

January 2000

Theoretical study on x-ray spectra from dense plasmas

（高密度プラズマからのX線スペクトルに関する理論的研究）

Takeshi NISHIKAWA

January 2000

内容梗概

本論文は、著者による高密度プラズマからのＸ線スペクトルに関する理論的研究をまとめたものである。

近年、レーザー生成プラズマからのＸ線が注目されている。金などの高Ｚ物質に短波長レーザーを照射することにより、注入したエネルギーの半分以上を軟Ｘ線で取り出すことが可能であり、また低Ｚ物質に照射する場合は、その物質に特徴的な光子エネルギーのＸ線を高輝度で生成することが出来る。高Ｚプラズマからの軟Ｘ線は、高出力レーザーを用いることにより慣性核融合のドライバーとして、低Ｚプラズマからの軟Ｘ線はＸ線露光装置の光源などとしての応用が考えられている。

これらＸ線を光源として工学的に利用する上では、最終的な性能試験などには実験でプラズマからのＸ線のエネルギー、スペクトルをとる必要とされるであろうが、最適な光源設計の手段として、計算機コードによるシミュレーションは欠かせない存在となりつつある。

本論文では、レーザー生成プラズマのような、比較的高密度プラズマ中でのＸ線生成を流体コードを用いてシミュレーションする際に使用する原子モデルについて、モデルを構築、数値計算した。高Ｚ物質に照射する場合については、実際に流体コードに導入しシミュレーションを行った。

本論文は以下の４章より構成されている。

第１章は、緒論である。レーザー生成プラズマからの軟Ｘ線の実験、シミュレーションについて現在までの研究状況、シミュレーションで使用する原子過程で重要となる素過程、モデルをまとめた。その上で、本論文で扱う内容の、プラズマ中でのＸ線生成シミュレーションでの位置づけを、金などの高Ｚプラズマと電離の進んだプラズマの場合について明らかにした。

第２章では、レーザー生成高Ｚプラズマからの軟Ｘ線生成のシミュレーションにおける原子モデルについて述べた。金などの高Ｚ物質に短波長、高強度レーザーを照射することにより高効率で軟Ｘ線を生成することが出来ることが実験的に知られている。従来の流体コードによるシミュレーションではエネルギー変換効率は精度よく再現できるが、Ｘ線スペクトルはうまく再現できなかった。方位量子数を遮蔽水素モデルの電子エネルギー準位に導入し、従来より問題となっていた平均イオンに対するラインプロファイルのモデルを作成した。このモデルでＸ線の吸収係と放射係数を計算することにより、比較的簡単で計算量の少ない流体シミュレーションでありながら、実験と比較できるＸ線スペクトルを計算出来るようになった。また、このモデルで水素や炭素プラズマなどの低Ｚプラズマのオパシティーを計算、詳細なオパシティーコードと比較、検討した結果、比較的簡単な計算でありながら、精度よく計算できていることが確認された。また、このモデルの不十分な点を明らかにした。

第３章では、比較的電離が進んだプラズマからのＸ線スペクトルを扱う場合の原子モデルについて述べた。これらのイオンからの線スペクトルは古くからプラズマ診断の道具として用いられてきたため、たくさんのデータ、理論の蓄積がある。しかしながら、水素様、ヘリウム様、リチウム様イオン以外のイオン種については未だ、シミュレーションコードで用いるための原子モデルとしては十分な取り扱い方法が確立されていない点が数多くある。スペクトルを計算する上で重要となる電子のエネルギー準位は、たくさんの計算、実験結果が出版されている。しかしながら、それらは誤差を必ず含んでおり、適応範囲などが明らかでない場合が多い。その中から、いかにして最も信頼できるデータを選択するかについて新しい手法を提案した。プラズマ効果は、今なお、問題によっては未だモデルの未確立な部分が存在する。高励起状態数という視点からプラズマ効果を考察し、新しい簡便な式を導出した。

第４章は結論であり、以上の研究において得られた結果をまとめ本論文の総括とした。

Contents

Chapter 1

Introduction

After laser was invented in 1960, the wavelength becomes shorter, and engineering has achieved the high efficiency and high power[1]. By the irradiation of high-intensity laser light, we can easily make high energy-density plasmas. Usually, the plasmas emit high intensity X-rays. Since the electron-collisional excitation rate is proportional to the reciprocal of the transition energy and the radiative decay rate is proportional to the square of the transition energy, bound electrons are collisionally excited and radiatively decay in plasmas. Free electrons in a plasma, and large energy gap between excited states and ground state enable the high efficiency of energy conversion from laser to X-ray.

There are a lot of free electrons in a high-Z plasma, so that almost all laser energy can be efficiently absorbed into the plasma by the classical absorption (inverse-bremsstrahlung). The electronic levels of the high-Z ions are so complicated and so many that emitted X-ray from ions are not so much re-absorbed by the other ions in the plasma. As a result, relatively high conversion rate will be achieved farther in high-Z plasmas. When high-Z materials like gold is irradiated by the laser light of which intensity is $10^{13} \sim 10^{15}$ W/cm^2 and wavelength $0.26 \sim 0.35$ μm, more than one half of the absorbed energy is converted into soft X-ray as shown by experiments[2, 3, 4]. In Fig. 1.1, the typical X-ray conversion rate as a function of the laser intensity is shown. Gold is the converter material. Experimental results are marked with black, while the corresponding simulation is marked with open ones.

There are many applications for the soft x-ray: for example, indirectly driven inertial confinement fusion[5]. Many experiments have been carried out to study the X-ray conversion rate, and spectrum, and sophisticated hydrodynamic codes have been used to analyze the experimental results[3, 4]. By the simulations using the hydrodynamic codes, the X-ray conversion rate, defined as total X-ray energy divided by absorbed laser energy can well be reproduced. However, the X-ray spectra by the simulations do not coincide with the corresponding experimental ones. For the practical application, not only the amount of the X-ray emission but also the x-ray spectra from the plasma is sometimes required. Since the electron energy level of high-Z ions like gold is so complex and so many that appropriate atomic model, i.e., opacity and emissivity for hydrodynamic codes are required to reproduce the detailed X-ray spectrum.

In Chap. 2, we show a new atomic model for calculating the spectral opacity and emissivity of high-Z plasmas. Gold plasmas are mainly treated in this thesis; however, the atomic model can be applied to the other elements. Simply gold is a typical high-Z element, so that a lot of experimental results can be available for comparison study. The spectral opacity and emissivity are essentially important in solving the radiative transfer

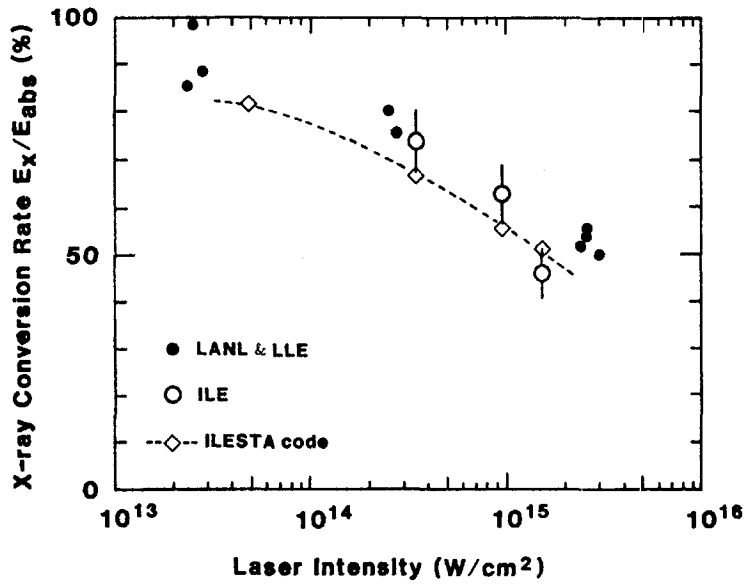

Figure 1.1: X-ray conversion rate as a function of the laser intensity. Wavelength of the laser is 0.35 μm. Gold is the converter material. Experimental results are marked with black, while the corresponding simulation is marked with open ones.

in the hydrodynamic code. In usual hydrodynamic codes, the average ion model in which the principal quantum number n is only taken into account in the electron energy levels has been widely used. In the new atomic model for high-Z plasmas, we take into account not only the principal quantum number n, but also the azimuthal quantum number l in the electron energy levels. We also give a solution for the difficulty whenever we meet if we use the average ion model, i.e., the line profile modeling for the average ion.

We treat the atomic model of highly ionized ions in Chap. 3. Main applications are line spectra from highly ionized plasmas: for example, line spectra due to the impurity in laser imploded plasmas, and X-ray spectrum from stellar plasmas. If number of bound electron in the open-shell becomes larger than three, or smaller than $(2n^2-3)$, number of possible terms of energy levels suddenly increase, so that main objectives are H-like, He-like, and Li-like ions. In the inertial confinement fusion research, spectroscopic measurements of X-ray from imploded plasmas more than solid density has have been carried out[7, 8]. Recently, new interest in opacity of stellar plasmas has arisen and precise opacity experiments have been carried out[6]. In order to know density and/or temperature of the plasma, spectroscopic measurements have been widely used in experiment. A lot of detailed experimental results, for example, line profiles has been collected[9, 10]. Even commercial software for analyzing X-ray spectra from plasmas is also available[11]. Essentially important point in the analysis of X-ray spectra from these plasmas are that precise theoretical modeling and numerical calculations are required for understanding the experimental results. Practically, we need modeling of the plasma effect in atomic processes, atomic data for the elementary processes, calculation of the line profile of each line spectrum or modeling on the line profile for the atomic model, etc.

For energy level and oscillator strength, using a detailed atomic code like the GRASP[7], we can obtain fairly accurate data of isolated ions. Numerical values of experimental data

and results of atomic code are also available in literature, for example, Kelly's table[8] and the Opacity Project book by Seaton[9]. However, above-mentioned sets of data are sometimes not enough for building up models of atomic process in the plasmas. From the Grotrian diagram, only data for the dipole allowed transition are available, but the line strength is sometimes strongly affected by the states which are not available.

There are still difficult points for some purposes in treating plasma effects. Among them, we discuss a problem that we always meet when we want to build up a model of atomic process, i.e. cutting off the highly excited states, is discussed and simple estimation for that is shown.

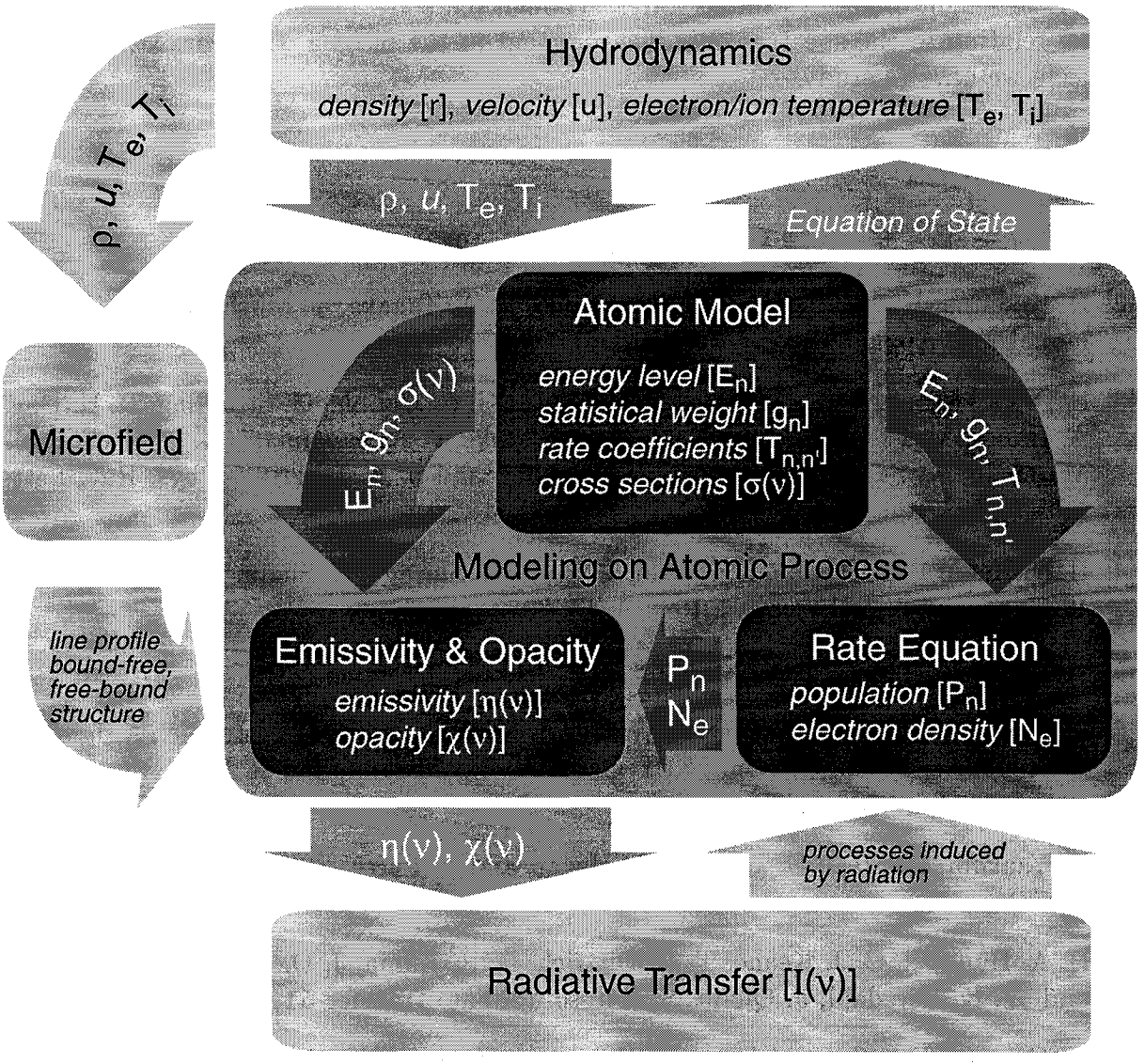

Figure 1.2: Atomic physics treated in this thesis. The Darken areas are treated.

Finally using Fig. 1.2, we explain the atomic physics treated in this thesis. The Darken areas are treated. In the simulation of X-ray generation in plasmas, hydrodynamics, population kinetics of ions, and radiative transfer in the plasma are solved numerically. If we can assume that the plasma is in the LTE, the relation like the Saha-Boltzmann determines population. If not, rate equation should be solved. In most cases, we can assume a certain quasi-steady state approximation even in the non-LTE case. In Chap. 2, we

assume the collisional radiative equilibrium[12] for the population. Although the average ion model and the screened hydrogenic model have been used as the atomic modeling for high-Z plasmas, we developed a new atomic model. In the model, we included the azimuthal quantum number l in the electron energy level within the framework of the average ion model and the screened hydrogenic model, and gave a solution for the line profile of the average ion.

In Chap. 3, we treated only the modeling of atomic processes in highly ionized plasmas. One is how to select the reliable data of electron energy levels of many ions from a lot of published ones. The other is the modeling of the plasma effect in view of the statistical weight of highly excited states. Though there are a lot of work on such atomic model relating to the spectroscopic measurement of the plasma, there are still a lot of subjects we have to study.

References

[1] 霜田光一, レーザー物理入門, (岩波書店, 東京, 1983)

[2] R. Kodama, K. Okada, N. Ikeda, M. Mineo, K. A. Tanaka, T. Mochizuki, and C. Yamanaka, J. Appl. Phys. **59**, 3050 (1986).

[3] P. D. Goldstone, S. R. Goldman, W. C. Mead, J. A. Cobble, G. Stradling, R. H. Day, A. Hauer, M. C. Richardson, R. S. Marjoribanks, P. A. Jaanimagi, R. L. Keck, F. J. Marshall, W. Seka, O. Barnouin, B. Yaakobi, and S. A. Letzring, Phys. Rev. Lett. **59**, 56 (1987).

[4] H. Nishimura, H. Takabe, K. Kondo, T. Endo, H. Shiraga, K. Sugimoto, T. Nishikawa, Y. Kato, and S. Nakai, Phys. Rev. A **43**, 3073 (1991).

[5] 高部英明, 三間圀興, 核融合研究 **68** 別冊, 13 (1992).

[6] P. T. Springer, D. J. Fields, B. G. Wilson, J. K. Nash, W. H. Goldstein, C. A. Iglesias, F. J. Rogers, J. K. Swenson, M. H. Chen, A. Bar-Shalom, and R. E. Stewart, Phys. Rev. Lett. **69**, 3735 (1992).

[7] B. Yaakobi, D. Steel, E. Thorsos, A. Hauer, and B. Perry, Phys. Rev. Lett. **39**, 1526 (1977).

[8] B. A. Hammel, C. J. Keane, T. R. Dittrich, D. R. Kania, J. D. Kilkenny, R. W. Lee, and W. K. Levedahl, J. Quant. Spectrosc. Radiat. Transfer **51**, 113 (1994).

[9] H. Griem, 1974, *Spectral Line Broadening by plasmas* (New York: Academic Press).

[10] 山本学, 村山精一, プラズマの分光計測, (学会出版センター, 東京, 1990).

[11] R. W. Lee, *User Manual for RATION*, (Lawrence Livermore National Laboratory, 1990).

[12] W. A. Lokke, and W. H. Grasberger, Lawrence Livermore National Laboratory Report No. UCRL-52276, 1977

Chapter 2

X-ray spectra from high-Z plasmas

2.1 Introduction

When an intense laser light ($\sim 10^{14}$ W/cm^2) of short wavelength ($0.26 \sim 0.35$ μm) irradiates on a high-Z material, more than 50 % of the absorbed energy is converted into soft X-rays as observed in experiments[1]. There are many applications for the soft X-ray: for example, indirectly driven inertial confinement fusion[2] and efficient and convenient X-ray source. Many experiments have been carried out to study the X-ray conversion rate, and spectrum, and sophisticated hydrodynamic codes have been used to analyze the experimental results[3, 4]. The simulations using the hydrodynamic codes can well be reproduce the X-ray conversion rate, defined as total X-ray energy divided by absorbed laser energy. However, the X-ray spectra by the simulations do not coincide with the corresponding experimental ones. In this chapter, we show a new atomic model for calculating the spectral opacity and emissivity of high-Z plasmas. Gold plasmas are mainly treated in this thesis; however, the atomic model can be applied to the other elements. Simply gold is a typical high-Z element, so that a lot of experimental results can be available for comparison study. The spectral opacity and emissivity are essentially important in solving the radiative transfer in the hydrodynamic code. In usual hydrodynamic codes, the average ion model in which the principal quantum number n is only taken into account in the electron energy levels has been widely used. In the new atomic model for high-Z plasmas, we take into account not only the principal quantum number n, but also the azimuthal quantum number l in the electron energy levels. We also give a solution for the difficulty whenever we meet if we use the average ion model, i.e., the line profile modeling for the average ion.

In Sec. 2.2, models which are usually used in laser plasma simulations are summarized. We explain the average ion model, the screened hydrogenic model (SHM), detail of the rate coefficients, models for the pressure ionization and the continuum lowering, the collisional radiative equilibrium model (CRE), the local thermodynamic equilibrium model (LTE), and detail of formulae for the emissivity and opacity calculations

In Sec. 2.3, we show the importance of the inclusion of the azimuthal quantum number in the electron energy levels for partially ionized high-Z plasmas. A spectral emissivity with the electron energy level in which the principal quantum number and the azimuthal quantum number are taken into account is calculated and compared with that obtained without the azimuthal quantum number.

The spectral opacity and emissivity calculated by the average ion model are relatively simple, spend less computation time, so that application to hydrodynamic codes has

been easily done. But there always exists a difficulty in solving radiation transport in hydrodynamic codes because the spectral opacity and emissivity are calculated as those of one fictitious ion of averaged charge. In Sec. 2.4, we show a line profile modeling of the opacity and emissivity in the average ion model. In the modeling, the effective line width is estimated by the distribution of the line group stems from the different charge-state. The new spectral opacity and emissivity are calculated to install in a hydrodynamic code ILESTA-1D and a numerical simulation for a gold plasma is carried out and compared with its experimental result.

In Sec. 2.5, we show the accuracy and limitation of this opacity and emissivity model. We compare the electron energy level and the oscillator strength used in the model to those by the Hartree-Fock-Slater model. The ionic distribution of each charge state by the statistical model with which the effective line width is estimated is compared with the result by the detailed configuration accounting model for the aluminum plasma. Based on the statistical model, detailed spectral opacities for the plasmas including low-Z elements can be calculated and have been compared with the results by detailed opacity codes and experimental results.

2.2 Models for opacity and emissivity calculations

In this section, models that have been widely used in laser plasma simulations are summarized.

2.2.1 Average ion model

The population in a plasma will be determined if the rate equations for the ions of all charge states and all excited states could be solved. The word population is used for the number density of ions with different electronic configuration. For the high-Z plasmas, however, it is practically impossible to solve all of the rate equations due to many charge states and excited states, so that an appropriate simplification is required[5, 6]. For the case of laser produced plasmas, the average ion model has been widely used. In Fig. 2.1, the average ion model is shown schematically. In this model, rate equations are solved for one fictitious hydrogenic ion including an averaged number of bound electrons for each level, instead of solving the rate equations for all ions of different electronic configuration. The models in which the principal quantum number is taken into account in the electron energy level have been widely used for the rate equations of one fictitious ion. Hereafter, a fractional number of electrons in the level k of the average ion model is called the fractional population.

The rate equation for the fractional population P_k in the level k of the average ion model can be written by

$$\begin{aligned}\frac{dP_k}{dt} &= T_{ck}V_k - T_{kc}P_k + \sum_{k'>k}\left(T^{\mathrm{D}}_{k'k}P_{k'}V_k - T^{\mathrm{U}}_{kk'}P_kV_{k'}\right) \\ &+ \sum_{k'<k}\left(T^{\mathrm{U}}_{k'k}P_{k'}V_k - T^{\mathrm{D}}_{kk'}P_kV_{k'}\right) \qquad (2.1)\end{aligned}$$

where $V_k = 1 - P_k/D_k$ is the vacancy of the level k. D_k is the statistical weight of the level k. If k is the principal quantum number, $D_n = 2n^2$. T_{ck} and T_{kc} are the rate for the recombination from the free state and the ionization from the level k, respectively.

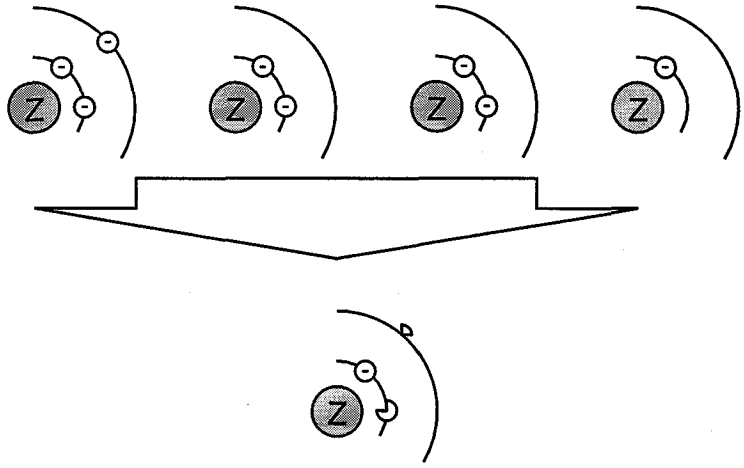

Figure 2.1: Schematic figure of the average ion model.

$T^{\mathrm{D}}_{k'k}$ and $T^{\mathrm{U}}_{k'k}$ are the rate of the deexcitation from the level k' to the level k and the excitation from the level k' to the level k, respectively. In a plasma, due to such various mechanisms as electron collisional and radiative processes, recombination, ionization, deexcitation and excitation occur, i.e.

$$\begin{aligned} T_{kc} &= T^{\mathrm{CD}}_{kc} + T^{\mathrm{RD}}_{kc} + T^{\mathrm{DD}}_{kc}, \\ T_{ck} &= T^{\mathrm{CU}}_{ck} + T^{\mathrm{RU}}_{ck} + T^{\mathrm{AU}}_{ck}, \\ T^{U}_{k'k} &= T^{\mathrm{CU}}_{k'k} + T^{\mathrm{RU}}_{k'k}, \\ T^{D}_{k'k} &= T^{\mathrm{CD}}_{k'k} + T^{\mathrm{RD}}_{k'k}. \end{aligned}$$

T^{CD}_{kc}, T^{RD}_{kc}, and T^{DD}_{kc} are the three body collisional recombination, the radiative recombination, and the dielectronic recombination, respectively. T^{CU}_{ck}, T^{RU}_{ck}, and T^{AU}_{ck} are the electron collisional ionization, the radiative ionization, and the autoionization, respectively. $T^{\mathrm{CU}}_{k'k}$ and $T^{\mathrm{RU}}_{k'k}$ are the electron collisional excitation and the radiative excitation, respectively. $T^{\mathrm{CD}}_{k'k}$ and $T^{\mathrm{RD}}_{k'k}$ are the electron collisional deexcitation and the radiative decay, respectively.

2.2.2 Screened hydrogenic model (SHM)

If the electronic configuration of an atom or ion is determined, the energy level (ionization potential) of a bound electron can be calculated theoretically, using for example, Hartree-Fock-Slater method[7]. In the simulation of the laser-produced plasma, however, the average ion model with a fractional number of electrons in the levels is used for solving the rate equations of one fictitious hydrogenic ion. For such situation, the screened hydrogenic model (SHM) is the best fit.

Figure 2.2 is the schematic figure of the screened hydrogenic model (SHM). In the SHM, using the screening constant that represents an extent to which an electron in the lower level shields the nuclear charge, energy levels of non-hydrogenic ion can be expressed by the hydrogenic energy level with the shielded nuclear charge. In this subsection, we show the SHM by More[8]. If the fractional population P_n for all levels are determined,

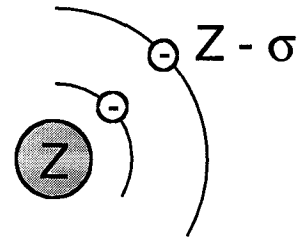

Figure 2.2: Schematic figure of screened hydrogenic model (SHM).

the effective charge Z_n which is the effective charge the electron in the level n feels is

$$Z_n = Z - \sum_{n'<n} \sigma_{nn'} P_{n'} - \frac{1}{2}\sigma_{nn} P_n, \tag{2.2}$$

and the electron energy level E_n is

$$E_n = -\frac{{Z_n}^2}{2n^2} + \frac{Z_n}{2n^2}\sigma_{nn} P_n + \sum_{n'>n} \frac{Z_{n'}}{n'^2}\sigma_{n'n} P_{n'} \qquad \text{(Ry)} \tag{2.3}$$

where Z is the nuclear charge (atomic number), and $\sigma_{nn'}$ is the screening constant. The set of the screening constants calculated by More is widely used in the calculation of the opacity and emissivity, and of the equation of state in hydrodynamic codes, since the model fulfills the thermodynamic consistency when applied to plasmas. More's set of the screening constant is shown in Table 2.1

Table 2.1: More's set of the screening constants

n	1	2	3	4	5	6	7	8	9	10
1	0.3125	0.9380	0.9840	0.9954	0.9970	0.9970	0.9990	0.9990	0.9999	0.9999
2	0.2345	0.6038	0.9040	0.9722	0.9979	0.9880	0.9900	0.9990	0.9999	0.9999
3	0.1093	0.4018	0.6800	0.9155	0.9796	0.9820	0.9860	0.9900	0.9920	0.9999
4	0.0622	0.2430	0.5150	0.7100	0.9200	0.9600	0.9750	0.9830	0.9860	0.9900
5	0.0399	0.1597	0.3527	0.5888	0.7320	0.8300	0.9000	0.9500	0.9700	0.9800
6	0.0277	0.1098	0.2455	0.4267	0.5764	0.7248	0.8300	0.9000	0.9500	0.9700
7	0.0204	0.0808	0.1811	0.3184	0.4592	0.6098	0.7374	0.8300	0.9000	0.9500
8	0.0156	0.0624	0.1392	0.2457	0.3711	0.5062	0.6355	0.7441	0.8300	0.9000
9	0.0123	0.0493	0.1102	0.1948	0.2994	0.4222	0.5444	0.6558	0.7553	0.8300
10	0.0100	0.0400	0.0900	0.1584	0.2450	0.3492	0.4655	0.5760	0.6723	0.7612

2.2.3 Rate coefficients in the average ion model

The typical rate coefficients used in the simulation of laser produced plasmas are summarized in Ref. [6, 9, 10, 11]. For the rate coefficient of the electron collisional ionization, the Seaton's formula[10],

$$T_{kc}^{\mathrm{CU}} = 6.80 \times 10^{-11} {T_e}^{-3/2} N_e {u_k}^{-2} \exp(-u_k) \qquad (\mathrm{sec}^{-1})$$

is used where T_e and N_e are the electron temperature in unit of keV and the number density of the plasma in unit of cm^3, respectively. $u_k = |E_k|/T_e$ where E_k is the ionization potential of the electron in the level k.

For the rate coefficient of the electron collisional excitation, the Bethe approximation using the Gaunt factor[6],

$$T_{kk'}^{CU} = 5.00 \times 10^{-10} N_e T_e^{-3/2} u_{kk'} \exp(-u_{kk'}) G_{kk'} f_{kk'} \qquad (\sec^{-1}),$$

is used where $u_{kk'} = |E_k - E_{k'}|/T_e$. If the k is the principal quantum number,

$$G_{nn'} = 0.19 \left[1 + 0.9 \left\{ 1 + \frac{n'(n'-n)}{20} \left(1 - \left(1 - \frac{2}{Z} \right) u_{nn'} \right) \right\} \exp(u_{nn'}) E_1(u_{nn'}) \right],$$

where

$$E_1(x) = \int_x^\infty \frac{e^{-y}}{y} dy.$$

Values of the hydrogenic oscillator strength could be found in Table 13 of Ref. [12]. An approximate formula

$$\exp(x) E_1(x) = \ln\left(\frac{x+1}{x} \right) - \frac{0.4}{(1+x)^2}$$

is used for the calculations. More detailed numerical formula can be found in Ref. [10].

The three-body collisional recombination rate T_{kc}^{CD} and the collisional deexcitation rate $T_{k'k}^{CD}$ are derived with the principle of the detailed balance relation. In the local thermodynamic equilibrium (LTE) limit, the collisional processes balance each other;

$$\begin{aligned} T_{ck}^{CD} V_k^0 &= T_{kc}^{CU} P_k^0 \\ T_{kk'}^{CU} P_k^0 V_{k'}^0 &= T_{k'k}^{CD} P_{k'}^0 V_k^0, \end{aligned}$$

where the superscript 0 means the value in the LTE. The population in the LTE will be shown in Sec. 2.2.5.

2.2.4 Pressure ionization and continuum lowering

In laser produced plasmas, high density and low temperature are sometimes realized. In this case, the orbit radii of bound electrons become comparable to the ion sphere radius, and as a result, the pressure ionization and the continuum lowering occur. The pressure ionization is due to the disappearance of bound states. Even in low-density plasmas, the electron energy levels are shifted to the red side (lower energy side). In dense plasmas, due to the potential of the nearby ions, energy levels are strongly shifted to the red side; the continuum level is lowered.

The model by Zimmerman and More[13] is usually used to describe the continuum lowering and the pressure ionization.

The continuum lowering is expressed by the reduction of the ionization potential

$$\Delta E = \frac{9}{5} \frac{Z_e}{R_0} \qquad (\text{AU})$$

where R_0 is the ion sphere radius in atomic unit. R_0 is defined by

$$\frac{4}{3} \pi R_0^3 N_i = 1$$

and Z_e is the average ionization degree of the plasma and the definition in the average ion model will be shown in Eq. (2.6). The pressure ionization is expressed by the decrease of the statistical weight of the level. In the model, the statistical weight of the hydrogenic ion is expressed by

$$D_n = {D_n}^0 \Big/ \left[1 + \left(\alpha \frac{{r_n}^0}{R_0}\right)^\beta\right]$$

where ${D_n}^0$ is the statistical weight of the isolated ion. In the case of the hydrogenic ion, ${D_n}^0 = 2n^2$. ${r_n}^0$ is the orbital radius of the neutral atom expressed by

$${r_n}^0 = \frac{n^2}{Z_n} \qquad \text{(AU)}.$$

α and β are adjustable parameters to be selected for the ionization degrees in the low-temperature and high-density limit to be those by the Thomas-Fermi model. In the case of gold plasma, $\alpha = 2$ and $\beta = 4$ are used[14]. In Ref. [13], they have used the orbital radii of neutral atom instead of that of the ion in the plasma. Figure 2.3 shows the difference between the two models where the electron temperature is 10 eV in both cases. Figure 2.3 (a) shows the results by the original description by Zimmerman and More, in which the orbital radii of the neutral atom are used. Figure 2.3 (b) shows in contrast the results in which the orbital radii of the ion in the plasma are used instead.

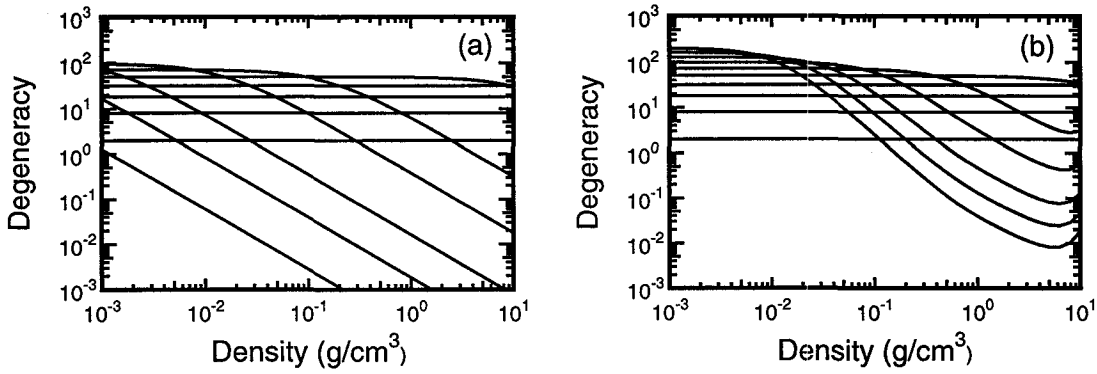

Figure 2.3: Statistical weight of bound states of the hydrogenic model in dense plasma where the temperature is 10eV in both cases. (a) Zimmerman and More's original model. The orbital radii of the neutral atom are used. (b) The orbital radius of the ion in the plasma is used instead.

From Fig. 2.3 we observe that, as the density increases, the statistical weight decreases from the highly excited states. In the case where the orbital radii of the ion in the plasma are used, the statistical weights do not monotonously decrease. When the pressure ionization occurs, the effective nuclear charge Z_n increases and the orbital radius decreases. As a result, the statistical weight increases. After that, the statistical weights again decrease.

Figure 2.4 shows the temperature dependence of the statistical weight. When the temperature increases, the plasma is highly ionized due to the electron collisional ionization, and the orbital radii are so small that its effect on the pressure ionization is reduced.

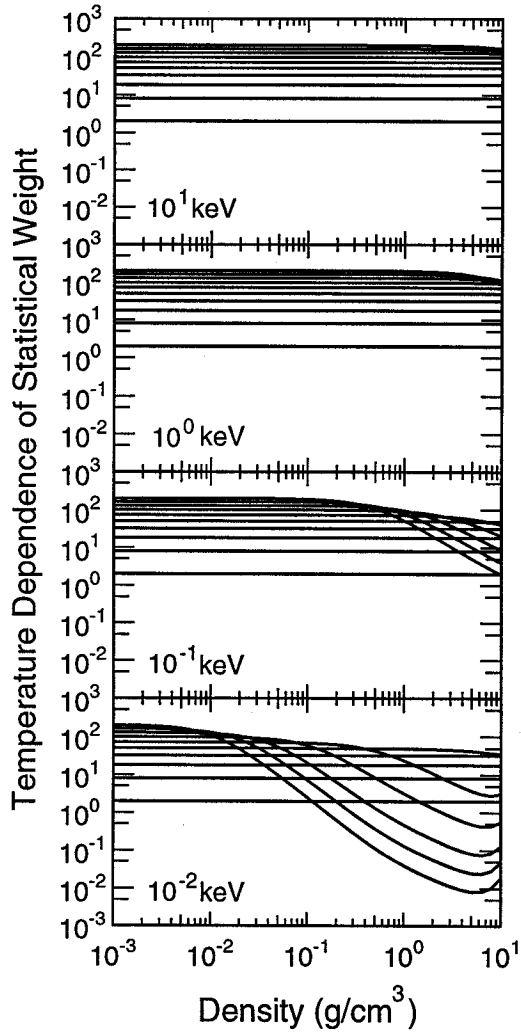

Figure 2.4: Temperature dependence of the statistical weight. The model with the orbital radius of the ion in the plasma are used instead of Zimmerman and More's original model.

Busquet[15] has used the coefficients $\alpha = 1$ and $\beta = 1$. As a result, the statistical weight becomes

$$\frac{D_n}{D_n{}^0} = \left(1 + \frac{r_n{}^0}{R_0}\right)^{-1} \sim \left(1 + \frac{\Delta E_n}{E_n{}^0}\right)^{-1} \sim 1 - \frac{\Delta E_n}{E_n{}^0},$$

where $E_n{}^0$ is the ionization potential of the isolated ion. The statistical weight disappears if the reduction of the ionization potential ΔE_n becomes equal to $E_n{}^0$. This behavior is very reasonable for the average ion model. Busquet proposed to use ΔE_n of the neutral atom.

We met a difficulty that the pressure ionization sometimes disappeared when we tried to use ΔE_n in the plasma instead of that of the isolated ion like what we did in the case of Zimmermann and More's model. Since the equation of the Busquet's model does not include the density, i.e., the pressure ionization is included through the continuum lowering, this strange phenomenon can be realized. As the continuum lowering can be zero even in a dense plasma numerically, the effect of the pressure ionization can be zero.

2.2.5 Local thermodynamic equilibrium (LTE) and collisional radiative equilibrium (CRE)

We can obtain the fractional population of the average ion model in the local thermodynamic equilibrium (LTE) by the Thomas-Fermi-Shell model[11]. In the model, using the Fermi-Dirac distribution

$$P_n = D_n \Big/ \left[1 + \exp\left(\frac{E_n - \mu}{k_{\mathrm{B}} T_{\mathrm{e}}}\right)\right] \tag{2.4}$$

and the number of free electrons by the Thomas-Fermi model

$$N_{\mathrm{e}} = N_{\mathrm{e}} N_{\mathrm{i}} = \frac{1}{2\pi^2}\left(\frac{2 m_{\mathrm{e}} k_{\mathrm{B}} T_{\mathrm{e}}}{\hbar^2}\right)^{3/2} I_{\frac{1}{2}}\left(\frac{\mu}{k_{\mathrm{B}} T_{\mathrm{e}}}\right) \tag{2.5}$$

where

$$I_{1/2}(x) = \int_0^\infty \frac{y^{1/2}}{1 + \exp(y - x)} dy$$

and

$$Z_{\mathrm{e}} = Z - \sum P_n, \tag{2.6}$$

the population for a given electron energy level is obtained. Here μ, k_{B}, $\hbar$, and m_{e} are the chemical potential, the Boltzmann constant, the Dirac constant defined by $h = \hbar/2\pi$, and the electron mass, respectively. h is the Planck constant. By the two iterative calculations, i.e., the Eqs. (2.4), (2.5), and (2.6) and the equation for the energy level of the SHM, i.e., Eqs. (2.2) and (2.3), the fractional population of the average ion model in the LTE can be obtained.

$I_{1/2}(x)$ is called the Fermi integral. A simple numerical formula is given by Latter[16]

$$I_{1/2}(x) = \frac{\sqrt{\pi}}{2} e^x \left(1 - \frac{e^x}{2^{3/2}} + \frac{e^{2x}}{3^{3/2}} - \frac{e^{3x}}{4^{3/2}} + \frac{e^{4x}}{5^{3/2}} - \frac{e^{5x}}{6^{3/2}} + \frac{e^{6x}}{7^{3/2}}\right)$$
$$(-\infty < x \leq -2.0)$$

$$
\begin{aligned}
&= 0.678091 + 0.53619667x + 0.16909748x^2 + 0.018780823x^3 \\
&\quad -0.0023575446x^4 - 0.000639610797x^5 \qquad (-2.0 \le x \le 0) \\
&= 0.678091x + 0.53638x + 0.16682335x^2 + 0.0206067x^3 \\
&\quad -0.00601491x^4 + 0.000490398x^5 \qquad (0 \le x \le 3.0) \\
&= 0.757064709 + 0.3922888x + 0.2705525x^2 - 0.01682933x^3 \\
&\quad +0.0008258364x^4 - 0.00001819771x^5 \qquad (3.0 \le x \le 10.0) \\
&= \frac{2}{3}x^{\frac{3}{2}}\left(1 + \frac{1.2337005}{x^2} + \frac{1.0654119}{x^4} + \frac{9.7015185}{x^6}\right. \\
&\quad \left. + \frac{242.71502}{x^8} + \frac{12313.691}{x^{10}}\right) \qquad (10.0 \le x \le 10^5) \\
&= \frac{2}{3}x^{3/2} \qquad (10^5 \le x \le \infty)
\end{aligned}
$$

In laser produced plasmas, due to the large mean free path of the X-ray compared with a size of the plasma, the LTE assumption for the plasma is not appropriate[6]. One of the non-LTE plasma model is the collisional radiative equilibrium (CRE) model in which all radiation are assumed to escape from the plasma and the electron temperature has been kept constant. Though the population of excited states decreases due to the radiative decay, the electron collision makes the excited population again. There is an energy flow from free electrons to the radiation field. This model is a good approximation for the population of excited states in optically thin plasmas, since a change in the plasma temperature is sometimes small enough.

Figure 2.5 shows the atomic processes that are taken into account in the CRE model, in which the atomic processes of the radiative recombination, the three-body collisional recombination, the collisional ionization, the radiative deexcitation, the collisional deexcitation, and the collisional excitation are taken into account. The rate equation of the average ion model Eq. (2.1) in which $T_{kc}^{\mathrm{DD}} = 0$, $T_{ck}^{\mathrm{RU}} = 0$, $T_{k'k}^{\mathrm{RU}} = 0$, and $T_{ck}^{\mathrm{AU}} = 0$ is solved for the steady state $dP_n/dt = 0$.

Figure 2.6 shows the density dependence of the fractional population of the average ion model in the CRE where the electron temperature is kept to be 500 eV. Material is gold ($Z = 79$). The ionization degree Z_{e} is not so different for each case. The detail of Z_{e} will be shown in Fig. 2.7. From Fig. 2.6 we see that, if the density is high enough, for example, 10 g/cm^3, the fractional population is almost the same as that in the LTE. The reciprocal of the slope is the temperature of the corresponding plasma. If the density is low enough, the radiative decay rate becomes much faster than that of the collisional excitation rate. As a result, the fractional populations of the lower excited states decrease. Even in the low-density region, the reciprocal of the slope of the highly excited states is still equal to the temperature of the plasma. This means that the highly excited electrons are thermodynamically equilibrated with the free electrons.

In Fig. 2.7, the equicontour of Z_{e} (averaged ionization degree) of the gold plasma in the CRE is compared with that in the LTE.

In the case of the LTE, with increasing plasma density, the ionization degree decreases due to the reduction of the density of states for free electrons. At high densities more than 1 g/cm^3 and low temperatures less than 100 eV, the ionization is enhanced because of the pressure ionization. Note that even gold plasma is calculated to be fully ionized at temperatures about 10 keV if we assume the LTE.

In the case of the CRE, even if the plasma temperature is higher than 10 keV, electron energy levels with principal quantum number less than or equal to two are

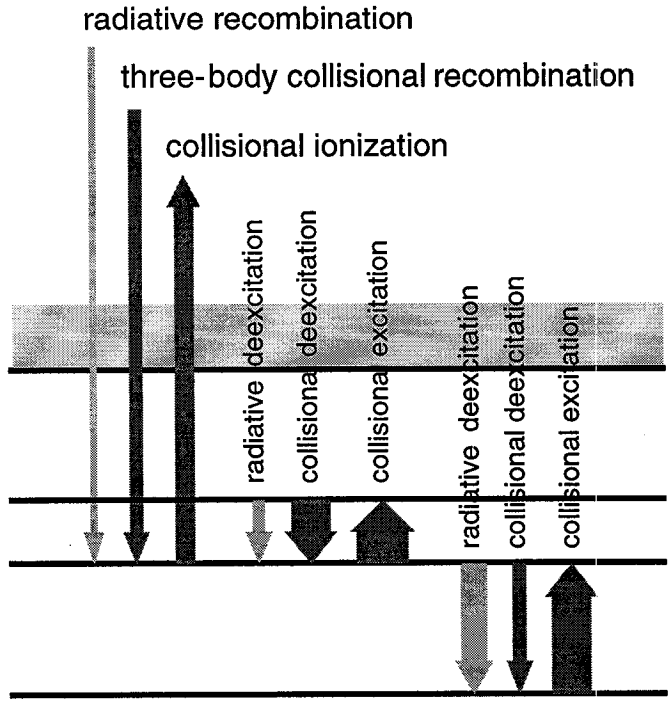

Figure 2.5: Atomic processes that are taken into account in the CRE model. The width of each arrow indicates the relative magnitude for the corresponding process.

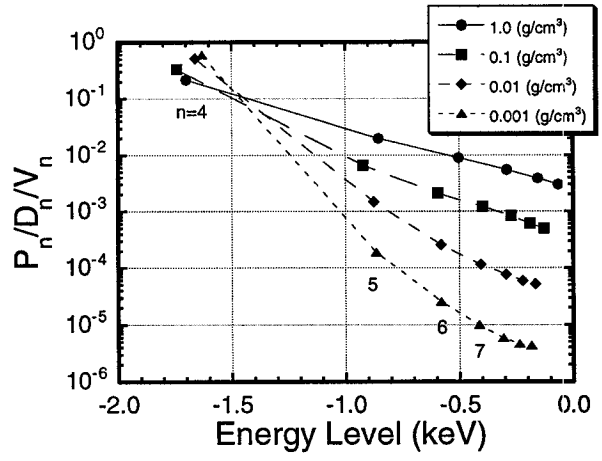

Figure 2.6: The density dependence of the fractional population of the average ion model in the CRE where the electron temperature is kept to be 500 eV. Material is gold ($Z = 79$).

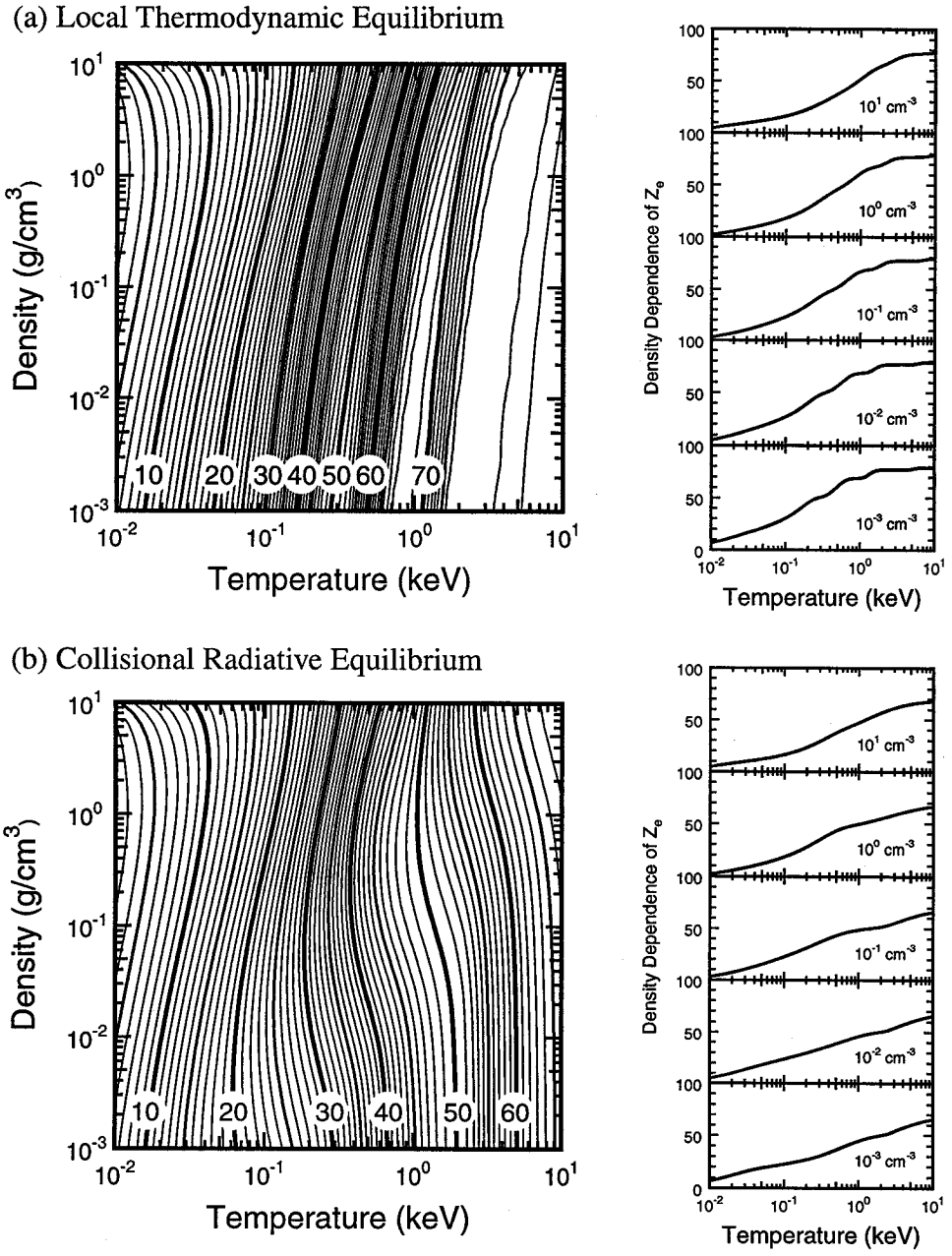

Figure 2.7: Equicontour of the Z_e (averaged ionization degree) of the gold plasma.

fully occupied. This is simply because of the large rate coefficients of the radiative decay to these levels compared with those of the collisional excitation and ionization. At high temperatures ($1 \sim 10$ keV) and low densities, the plasma is almost in the Coronal equilibrium, determined only by the electron temperature. As the plasma density increases further, the electron collisional process becomes dominant and tends to increase the ionization degree. At low temperatures ($10 \sim 100$ eV), the population is essentially determined by the collisional process and the LTE state is realized.

2.2.6 Formulas of the opacity and emissivity

Once the population is determined, the spectral opacity $\chi(\nu)$ and emissivity $\eta(\nu)$ can be calculated using the hydrogenic formulae. Here, ν is the frequency of the X-ray. There are three main processes by which a plasma emits or absorbs X-ray, i.e., the free-free, free-bound (bound-free), and bound-bound processes which are related to the rate coefficients and the scattering process, the effect of which is usually included in the opacity.

On establishing the formulae for the opacity and emissivity in average ion model, some of the formulae is derived by the relation among the Einstein coefficients $A_{n,n'}(\nu)$, $B_{n,n'}(\nu)$, and $B_{n',n}(\nu)$. The coefficients represent the spontaneous emission rate, the induced emission rate, and the absorption rate, respectively. Through the coefficients, the relation between the Planckian radiation (number of photons)

$$I(\nu) = \frac{2h\nu^3}{c^2} \Big/ \left\{ \exp\left(\frac{h\nu}{k_{\mathrm{B}}T_{\mathrm{e}}}\right) - 1 \right\}$$

and the bound electron distribution

$$P_{n'}V_nB_{n',n}(\nu)I(\nu) = \{A_{n,n'}(\nu) + B_{n,n'}(\nu)I(\nu)\}P_nV_{n'} \qquad (n' < n) \qquad (2.7)$$

is satisfied in the LTE.

From Eq. (2.7) and the relation between the fractional populations of different energy levels

$$\frac{P_n/V_n}{P_{n'}/V_{n'}} = \frac{D_n}{D_{n'}} \exp\left(-\frac{h\nu}{k_{\mathrm{B}}T_{\mathrm{e}}}\right), \qquad (2.8)$$

another relations among the Einstein coefficients

$$A_{n,n'} = \frac{2h\nu^3}{c^2} B_{n,n'} \qquad (2.9)$$

and

$$D_{n'}B_{n',n} = D_nB_{n,n'} \qquad (2.10)$$

are obtained.

For the emission by the free-free process, the simple formula of bremsstrahlung[17]

$$\eta_{\mathrm{ff}}(\nu) = \frac{8}{3}\left(\frac{2\pi}{3m_{\mathrm{e}}k_{\mathrm{B}}T_{\mathrm{e}}}\right)^{1/2} \frac{Z_{\mathrm{e}}e^6}{m_{\mathrm{e}}c^3} N_{\mathrm{i}}N_{\mathrm{e}} \exp\left(-\frac{h\nu}{k_{\mathrm{B}}T_{\mathrm{e}}}\right) g_{\mathrm{ff}}$$

is used where N_{i}, e, and c are the number density of ions, the electronic charge, and the speed of light, respectively. g_{ff} is the Gaunt factor for the free-free process, which reflects the difference between the quantum-mechanical and the classical calculations. It

increases in the low frequencies, but for the X-ray, it is not so important. As for the absorption, use of Eqs. (2.8), (2.9), and (2.10) yields

$$\chi_{\rm ff}^{\rm abs}(\nu) = \frac{P_n V_{n'} B_{n,n'}}{P_{n'} V_n A_{n',n}} \eta_{\rm ff}(\nu) = \exp\left(\frac{h\nu}{k_{\rm B} T_{\rm e}}\right) \frac{c^2}{2h\nu^3} \eta_{\rm ff}(\nu)$$

and

$$\chi_{\rm ff}^{\rm ind}(\nu) = \exp\left(-\frac{h\nu}{k_{\rm B} T_{\rm e}}\right) \chi_{\rm ff}^{\rm abs}(\nu) = \frac{c^2}{2h\nu^3} \eta_{\rm ff}(\nu).$$

For the free state, $D_{n'} = D_n$ is assumed.

The bound-free absorption cross section from level n to the free state is

$$\sigma_{nc} = \frac{2^6 \pi^4 e^{10} m_{\rm e} Z_n{}^4 g_{\rm bf}}{3\sqrt{3} c h^6 n^5 \nu^3} \qquad ({\rm cm}^2)$$

in the hydrogenic case[18]. Using the above we have

$$\chi_{\rm bf}^{\rm abs}(\nu) = \sigma_{nc} N_{\rm i} P_n V_{\rm c},$$

where $V_{\rm c}$ is the vacancy of the free state defined by

$$V_{\rm c} = 1 - \frac{P_{\rm c}}{D_{\rm c}} = \exp\left(\frac{E_{\rm c} - \mu}{k_{\rm B} T_{\rm e}}\right) \Big/ \left[1 + \exp\left(\frac{E_{\rm c} - \mu}{k_{\rm B} T_{\rm e}}\right)\right],$$

where $E_{\rm c} = h\nu - |E_n|$. Usually, $V_{\rm c} \sim 1$, because $E_{\rm c}$ is much larger than the chemical potential μ. If the plasma is dense enough, this assumption breaks down and the bound-free absorption is reduced by the factor $V_{\rm c}$. By Eqs. (2.9) and (2.10), we obtain the relations

$$\eta_{\rm fb}(\nu) = \sigma_{nc} \frac{2h\nu^3}{c^2} N_{\rm i} \frac{P_{\rm c}}{D_{\rm c}} D_n V_n$$

and

$$\chi_{\rm bf}^{\rm ind}(\nu) = \frac{c^2}{2h\nu^3} \eta_{\rm fb}(\nu).$$

The formula for the bound-bound emission is

$$\eta_{\rm bb}(\nu) = \frac{2\pi e^2}{m_{\rm e} c^3 h^2} N_{\rm i} P_{n'} V_n \frac{D_n}{D_{n'}} f_{nn'} (h\nu)^3 \phi(\nu), \qquad (n' > n).$$

$f_{nn'}$ denotes the absorption oscillator strength and $\phi(\nu)$ is a line profile function that satisfies $\int \phi(\nu)\, d\nu = 1$. By Eqs. (2.9) and (2.10), we also have

$$\chi_{\rm bb}^{\rm abs}(\nu) = \frac{\pi e^2}{m_{\rm e} c} N_{\rm i} P_n V_{n'} f_{nn'} \phi(\nu)$$

and

$$\chi_{\rm bb}^{\rm ind}(\nu) = \frac{c^2}{2h\nu^3} \eta_{\rm bb}(\nu).$$

Although the process of the induced emission is required for the fractional population to be the Fermi-Dirac distribution in the LTE limit, the effect in the opacity and emissivity calculation of laser produced plasmas is negligibly small.

The cross section of the simple Thomson scattering is expressed as

$$\sigma_{\mathrm{T}} = \frac{8\pi}{3}\left(\frac{e^2}{m_{\mathrm{e}}c^2}\right)^2$$

and therefore,

$$\chi_{\mathrm{s}}(\nu) = \sigma_{\mathrm{T}} N_{\mathrm{e}} = \frac{8\pi}{3}\frac{e^4}{{m_{\mathrm{e}}}^2 c^4} N_{\mathrm{e}}$$

is used for the formula of the scattering process in some cases. For the simulation of laser produced plasmas, the scattering process does not contribute a lot to the resultant spectral opacity and emissivity.

Figure 2.8 shows the emissivity of the gold plasma in the CRE model where the electron temperature is 200 eV and the density is 0.1 g/cm^3.

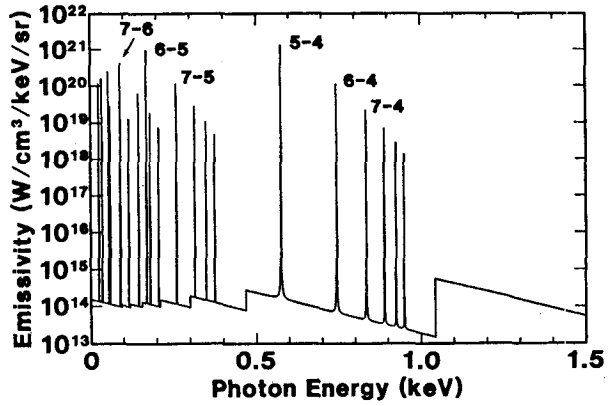

Figure 2.8: Emissivity of the gold plasma in the CRE model where the electron temperature is 200 eV and the density is 0.1 g/cm^3.

In order to show the relative intensity of the bound-bound transition, the Lorentzian profile

$$\phi^{\mathrm{L}}_{nn'}(E) = \frac{1}{\pi}\frac{W^{\mathrm{L}}_{nn'}}{(E - E_{nn'})^2 + (W^{\mathrm{L}}_{nn'})^2}$$

with

$$W^{\mathrm{L}}_{nn'} = 4.75 \times 10^{-6} {E_{nn'}}^2 \qquad \text{(keV)}$$

is used to plot Fig. 2.8.

2.3 l-splitting effect in spectral opacity and emissivity

In this section, we show the splitting of electron energy levels due to the difference in the azimuthal quantum number, i.e., the l-splitting effect. The SHM including the l-splitting is developed by Perrot[19].

In his model, the effective charge is

$$Z_n = Z - \sum_{n' \le n} P_{n'} \sigma_{nn'} \left(1 - \frac{1}{2}\delta_{nn'}\right) + \sum_{n'} P_{n'} q_{n'n} \sum_{l=0}^{n-1} x_{nl} g_{nl}$$

where $x_{nl} = P_{nl}/D_n$,

$$g_{nl} = \frac{1}{4n^2}[n^2 - 2l(l+1) - 1] + \nu_n,$$

and

$$q_{nn'} = \begin{cases} \frac{1}{\pi}\left(\frac{n'}{n}\right)^5 \left[2 - \left(\frac{n'}{n}\right)^2\right]^{1/2} & (2n^2 > n'^2) \\ 0 & (2n^2 \leq n'^2). \end{cases}$$

For the diagonal elements, the author has done a more accurate estimation using the exact hydrogenic wave functions.

The numerical values are shown in Table 2.2 for reference. If the l-splitting is neglected, $\sum_{l=0}^{n-1} x_{nl} g_{nl} = 0$.

Table 2.2: Numerical values of some of the constants needed in the SHM with l-splitting.

n	1	2	3	4	5	6	7
q_{nn}	0.270672	0.366310	0.371802	0.329523	0.295072	0.296580	0.320910
ν_n	0.000	0.070	0.020	0.012	−0.100	−0.400	−0.420

Using Z_n, the electron energy level including the l-splitting is

$$E_{nl} = E_n - \sum_{n'} P_{n'}[q_{nn'}S_{n'} - q_{n'n}S_n] - \frac{Z_n}{n^2} g_{nl} \sum_{n'} q_{n'n}$$

where

$$S_n = \frac{Z_n}{n^2} \sum_{l=0}^{n-1} x_{nl} g_{nl}.$$

E_n is the same expression as Eq. (2.3).

Figure 2.9 shows electron energy levels of the gold ions as a function of the number of bound electrons in the ground state. Figure 2.9 (a) shows the case without l-splitting (l-degenerate), while Fig. 2.9 (b) shows the case with l-splitting. From Fig. 2.9, we find that the electron energy level E_4 of Au^{+40}, for example, splits into four sublevels with the width of about 300 eV by including the l-splitting effect. As the number of bound electrons increases, the energy gaps between different principal quantum numbers decreases, while the energy split in the same principal quantum number increases. This shows that the l-splitting effect is more important in the partially ionized plasmas than in highly ionized plasmas.

The fractional population in the LTE and the resultant opacity and emissivity are obtained if electron energy levels including the l-splitting can be known. But on calculating the fractional population in the CRE, they are not sufficient. As shown in 2.2.3, we use the rate coefficients of the electron collisional ionization, and therefore, the three-body collisional recombination, which only depend on the energy level as the l-splitting effect, inclusion of the l-splitting in the atomic process is not so difficult. But for the electron collisional excitation and radiative decay, and therefore, the electron collisional deexcitation, it requires not only the energy level but also the oscillator strength between n, l sublevels. In this thesis, the oscillator strength of H-like ions for E_1, Li-like ions for E_2[20], Na-like ions for E_3[21], Cu-like ions for E_4[22] are used.

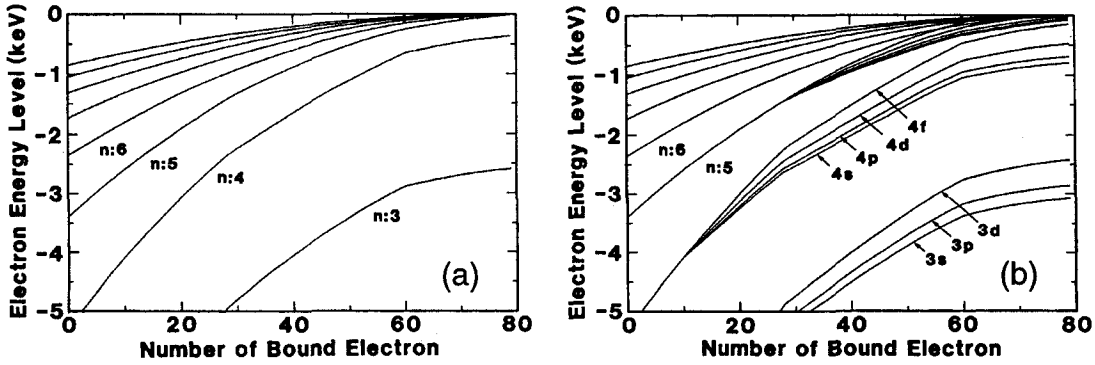

Figure 2.9: Electron energy levels of the gold plasma as a function of the number of bound electrons in the ground state. (a) Without l-splitting. (b) With l-splitting.

Figure 2.10 shows the fractional population divided by the statistical weight of the level. In the model, the l-splitting energy levels up to $n = 4$ are included. In the LTE, the fractional population is determined by the Fermi-Dirac distribution, i.e., the population imbalance between sublevels is determined by the energy differences. In the CRE, the population imbalance is determined by a magnitude of the radiative decay rate. As a result, the population imbalance becomes larger in the CRE than in the LTE due to the fact that the radiative decay rate of a state with larger azimuthal quantum numbers is larger.

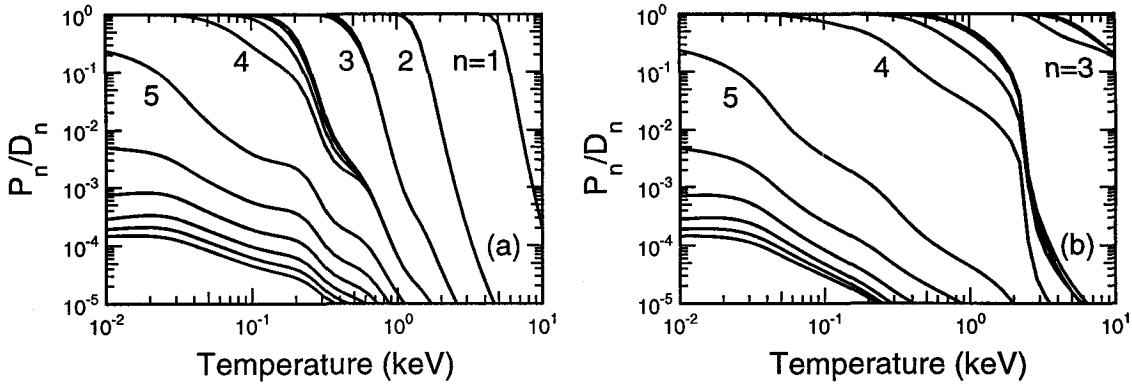

Figure 2.10: Electronic population of the average ion model divided by the statistical weight of the level. (a) Local thermodynamic equilibrium (LTE). (b) Collisional radiative equilibrium (CRE). l-splitting effect is more important in the CRE than in the LTE.

Figure 2.11 shows the emissivity of the gold plasma in the CRE including the l-splitting, where the electron temperature is 200 eV and the density is 0.1 g/cm^3. The corresponding figure without l-splitting was already given in Fig. 2.8

We remark that the relatively strong line emission due to the $4-5$ transition (about 570 eV) seen in Fig. 2.8 splits into three relatively strong lines due to the transitions of $4f-5g$ (about 520 eV), $4d-5f$ (about 730 eV), and $4p-5d$ (about 850 eV). The lines of $4d-5d$ (about 390 eV) and $4d-5p$ (about 630 eV) are relatively weak because of smaller oscillator strengths of these lines.

In Fig. 2.8, we can see that the relative intensity of the lines due to the $5-6$ transition

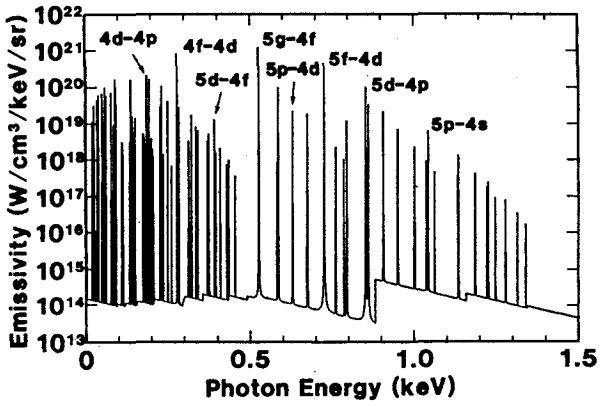

Figure 2.11: Emissivity of the gold plasma in the CRE model with l-splitting where the electron temperature is 200 eV and the density is 0.1 g/cm^3. The corresponding figure without l-splitting is shown in Fig. 2.8.

is as strong as that of line due to the $4-5$ transition. However, inclusion of the l-splitting reduces $5-6$ lines intensity. This is because of the line shift from $5-6$ transition of about 160 eV to $5g-6h$ transition of about 60 eV, which is the strongest among $5-6$ transitions when the l-splitting is included. Since the emissivity is proportional to the photon energy as $(h\nu)^3$, the intensity of $5g-6h$ transition decreases by a factor of $(60/160)^3 \sim 0.05$. The lines seen at about 280 and 180 eV are due to the $4d-4f$ and $4p-4d$ transitions, respectively. They are due to the transitions between sublevels for which the l-splitting is responsible.

2.4 Line profile modeling for X-ray transport

In the case of high-Z plasmas like gold treated in this thesis, the largest contribution to the global structure of the X-ray spectra is the l-splitting effect (hundreds eV) which has been already included in the model as shown in Sec. 2.3. Although the effect of the j-splitting (tens eV) has been predicted by theoretical calculation[23], in order to introduce the j-splitting, the development of a new SHM including the j-splitting is required.

Apart from the more precise treatment of the physical system of the average ion, we develop a line profile modeling for the average ion model. The difficulty encountered in applying the spectral opacity and emissivity based on the average ion model to a hydrodynamic code can be deduced the line profile modeling, since they are those of one *fictitious* ion of averaged charge. In this thesis, we propose a line profile for the average ion model of which widths are obtained by the line group structure of the same index in hydrogenic model, for example, $2-3$, $3-4, 4-5$, etc. The strength of the $2-3$ line in the average ion model, for example, reflects the contributions from the $2-3$ lines of Li-like through Ne-like ions in the reality. This estimation of the line width is natural for the basic line profile for the average ion model, since this information has been lost when we use the average ion model.

The model which enables to yield the population of different charge states from the fractional population of the average ion model was first proposed by Mayer[5], and an extension for the CRE by Ito *et al.*[10]. In this thesis, a simpler Mayer's statistical method is studied. In his model, the fractional population P_n in the level n of the average ion

model divided by the statistical weight D_n; $x_n = P_n/D_n$ is assumed to be the probability of the electron occupation in the level n. Then, the population of the ion which carries a different number of the bound electrons in the level n can be given by the binomial distribution. For example, the population of the ion $F_{P_4=5}$ which carries 5 electrons in the level of $n = 4$ is given by

$$F_{P_4=5} = {x_1}^2 {x_2}^8 {x_3}^{18} \frac{32!}{(32-5)!5!} {x_4}^5 (1-x_4)^{32-5} (1-x_5)^{50} \cdots \tag{2.11}$$

The comprehensive calculation had been done by Stein *et al.*[24].

Using the statistical method, we can estimate the population of each charge state. This is sometimes called the abundance of ions. Figure 2.12 shows the abundance in the gold plasma. Figure 2.12 (a) shows the case in the LTE, while Fig. 2.12 (b) shows the case in the CRE. The ionic charge states of the closed shell are dominant in certain temperature ranges at about 700eV $\sim$ 1.2keV for the Ne-like ($n = 2$), at about 250 $\sim$ 350eV for the Ni-like ($n = 3$), and at about 40eV for the Nd-like ($n = 4$) in the LTE, and at about 2 $\sim$ 2.6keV for the Ni-like, 45 $\sim$ 60eV for the Nd-like in the CRE, respectively. The structure due to the closed subshell of Pd-like ($4d^{10}$) can also be seen at about 350eV in Fig. 2.12 (b) and at about 100eV in Fig. 2.12 (a).

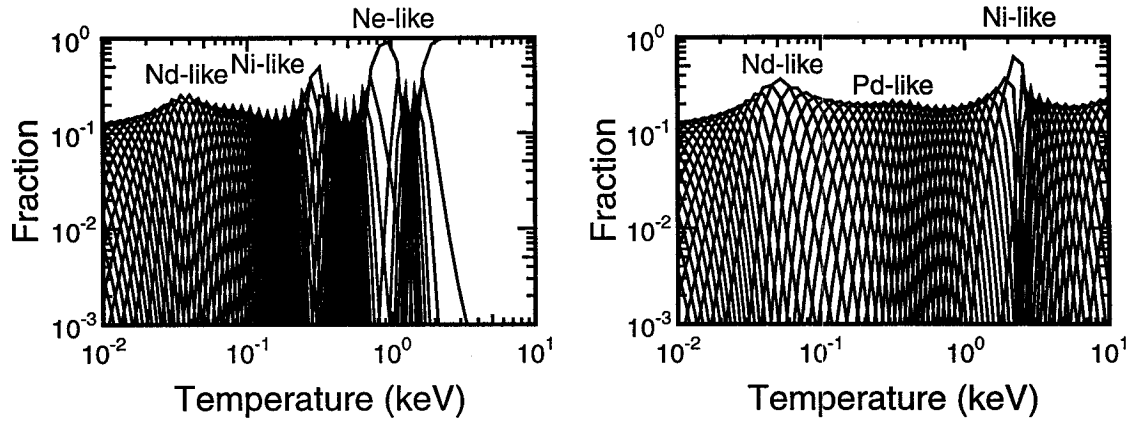

Figure 2.12: Ionic distribution of the different charge states estimated by the statistical method. The closed shell structure, dominant in certain temperature ranges can be seen. (a) Local thermodynamic equilibrium model. (b) Collisional radiative equilibrium model. The structure due to the closed subshell can be also seen.

At a given transition, the line position shifts according to a number of bound electrons, and the strength is weighted by the binomial distribution. In the case of large D_n the binomial distribution can be approximated by the Gaussian distribution. In real high-Z plasmas, this discreet structure of the line spectra is sometimes smeared out by another effects, for example, the term-splitting effect and the Stark effect. In this case, the line group profile of the transition from k to k' in the average ion model can be approximated by

$$\phi_{kk'}(E) = \frac{1}{\sqrt{2\pi} s \Delta E_{kk'}} \exp\left(\frac{(E - E_{kk'})^2}{2(s\Delta E_{kk'})^2}\right),$$

where $\Delta E_{kk'}$ is the energy shift of the line when the charge state changes by unity and s is the standard deviation defined by $s = P_n V_n$. The free-bound emissivity and bound-free opacity can be also obtained by the same idea as in the case of the bound-bound

transition. This line profile modeling is valid only in the LTE[25], the modeling is also used, however, in the CRE because the difference in the abundance between the LTE and CRE is assumed to be relatively small in the parameter region of the laser-produced plasmas treated here. In Fig. 2.13, the opacity of the gold plasma in the CRE is shown, where the electron temperature is 200 eV, and the density 0.01 g/cm^3. Figure 2.13 (a) shows the opacity of the one fictitious ion of the average ion model with the Lorentzian line profile. Figure 2.13 (b) shows the line group of the $4f - 5g$ transition, composed of lines from different charge states. The thick line profile in Fig. 2.13 (b) corresponds to the Gaussian profile, the half width of which is determined by the standard deviation of the line group.

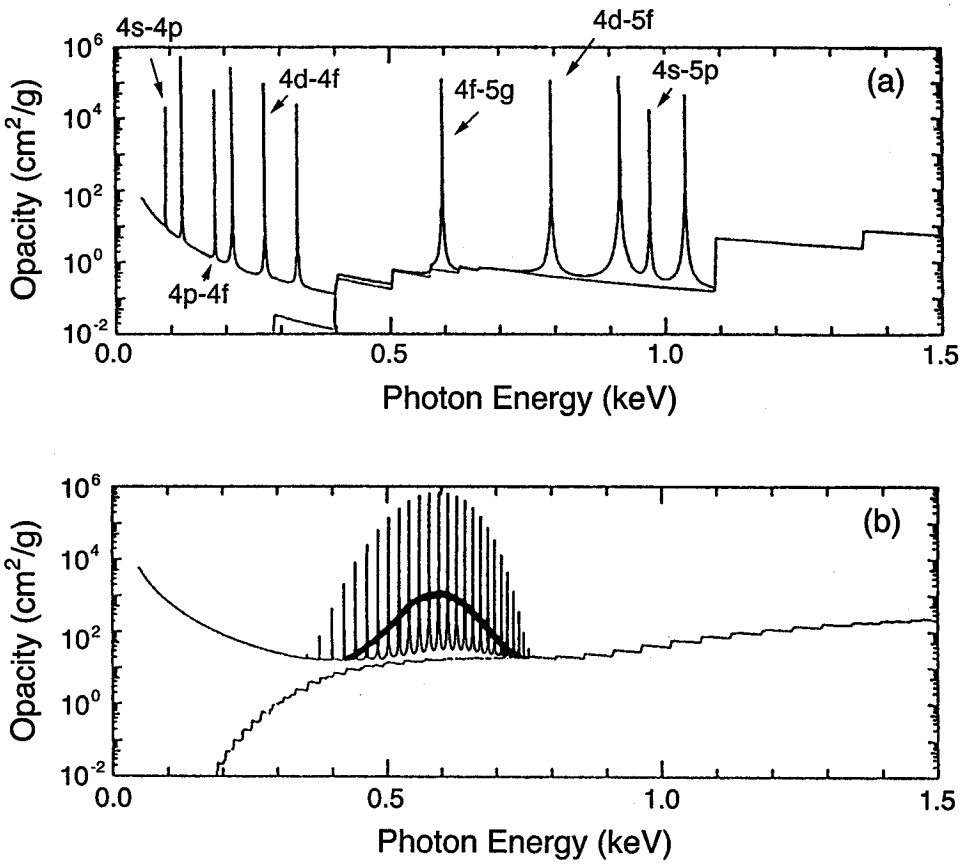

Figure 2.13: Opacity of the gold plasma in the CRE where the electron temperature is 200 eV, and the density 0.01 g/cm^3. (a) Simple Lorentzian line profile. (b) Line group of the $4f - 5g$ transition composed of lines from different charge states. The thick line profile corresponds to the Gaussian profile, the half width of which is determined by the standard deviation of the line group.

We showed two figures in Fig. 2.14 which shows the emissivity to be compared with Fig. 2.8 and 2.11. Figure 2.8 and 2.11 change their profile as shown in Figure 2.14. Figure 2.8 and 2.14 (a) illustrate the case without l-splitting, while Fig. 2.11 and 2.14 (b) are the case with l-splitting.

From Fig. 2.14 (a), the full width of the half maximum in the typical lines are about 100eV $(4-5)$, 165eV $(4-6)$, and 62eV $(5-6)$. In the simulation studied in Ref. [4], the effective line width of 150eV is assumed to reproduce the experimental X-ray conversion

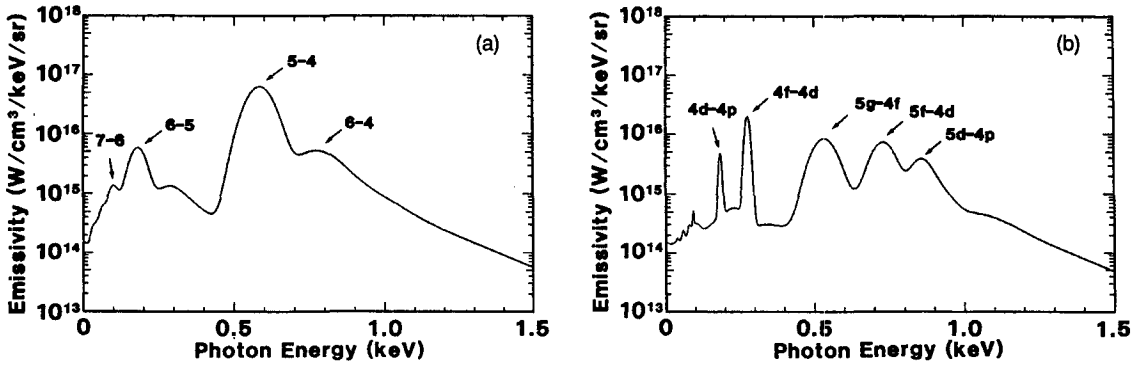

Figure 2.14: Emissivity of gold plasma in the CRE model, where electron temperature is 200 eV, and plasma density 0.1 g/cm^3. The line profile modeling is taken into account. (a) Without l-splitting. (b) With l-splitting.

rate. The above-mentioned line widths obtained by the statistical method give a physical basis for the effective line width of the simulation.

From Figure 2.14 (b), the full width at the half maximum in the typical lines are about 93 eV ($4f - 5g$), 86 eV ($4d - 5f$), and 19 eV ($4d - 4f$). The effective line widths of $\Delta n = 0$ transitions are relatively narrow, because the centers of these lines are not so affected by the change in the ionic charge state. For this plasma parameter, a number of electrons in the level of $n = 4$ changes. For the $4d - 4f$ transition, a number of electrons in the inner shell does not change. As a result, the position of the lines does not move. The line width due to the j-splitting is comparable to that determined by the statistical method[26, 23]. This effect will be discussed in Sec. 2.5.

By installing the spectral emissivity and opacity based upon the model shown above in the simulation code ILESTA-1D, a hydrodynamics simulation has been carried out. Figure 2.15 shows the time-integrated X-ray spectra observed in the laser irradiation side[4] where the experimental spectrum is shown by the solid line and the numerical one based upon a rather simple opacity modeling in which the principal quantum number n is only taken into account in the electron energy level is shown by the broken line. In the experiment, six beams with wavelength of 0.35 μm irradiates a large spot size (1 mm in diameter) with the intensity of 3.3×10^{14} W/cm^2 and the pulse duration of 800 ps. The beams are focused on a 0.436-μm-thick gold foil.

A typical feature is that the experimental spectrum has a strong peak near 200 eV and flat area in 400 $\sim$ 800 eV. The same structure in spectrum has also been observed in OMEGA experiment[3]. In contrast, the numerical spectrum of the original ILESTA-1D consists of two peaks: One is near 200 eV, which corresponds to line emissions due to the deexcitation into the level of $n = 4$, and the other is near 700 $\sim$ 800 eV, which corresponds to the line emissions due to the deexcitation into the $n = 5$ level. Clearly, the X-ray spectrum seen in the simulation is harder than that in the experiment.

Figure 2.16 shows the X-ray spectrum with the l-splitting effect. By comparing Fig. 2.16 with the numerical results shown in Fig. 2.15, the peaked spectrum at 700 $\sim$ 800 eV in Fig. 2.15 becomes flat due to the l-splitting and the peaked spectrum at 300 eV are due to the $\Delta n = 0$ transitions stemming mainly from the $4d - 4f$ transition.

There were simulations for the X-ray generation by laser produced plasmas with the l-splitting and either the LTE assumption[27] or the CRE assumption[28] model.

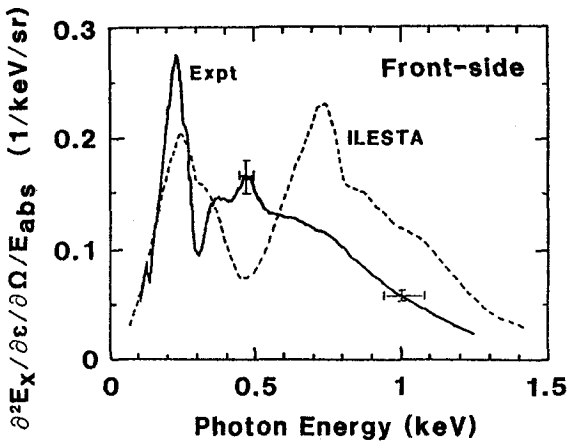

Figure 2.15: Time-integrated spectra of X-rays at the laser irradiation side where the experimental result is shown by the solid line and the simulation result by the broken line. The figure is taken from Ref. [4]. This is the case where six beams with wavelength of 0.35 μm irradiates a large spot size (1 mm in diameter) with the intensity of 3.3×10^{14} W/cm^2 and the pulse duration of 800 ps. The beams are focused on a 0.436-μm-thick gold foil.

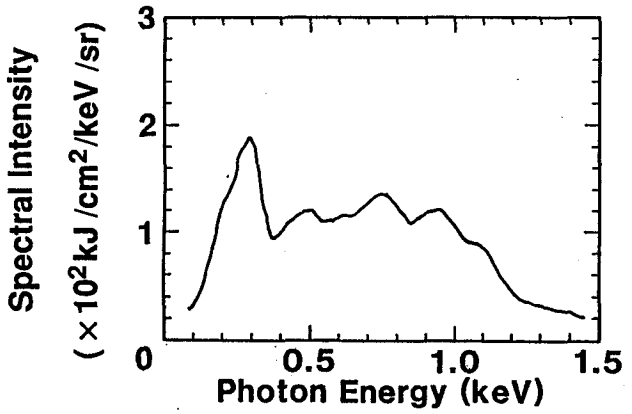

Figure 2.16: X-ray spectrum from the gold plasma calculated by the ILESTA-1D code, installing the new opacity and emissivity including the l-splitting effect.

In both simulations, they used the average ion model, but have failed to reproduce the corresponding experimental spectrum. From the above consideration, all of the CRE, the l-splitting effect, and the line profile modeling for the average ion model are important to reproduce the global structure of the X-ray spectrum of the corresponding experiment.

2.5 Accuracy and limitation

In this section, an accuracy of the atomic model used in Sec. 2.3 and 2.4 is examined in detail. From the content in this section, the limitation of the opacity and emissivity model will be clarified.

2.5.1 Energy level and oscillator strength

For the laser produced plasma like a gold plasma, atomic data of the level of $n = 4$ are the most important. For the electron energy level and the oscillator strength, the results by the Hartree-Fock-Slater (HFS) model[7] is used for reference. In the HFS model, the electronic structure is solved using the one electron approximation in the self-consistent field. The Schrödinger equation in the spherically symmetric potential $V(r)$ is written by

$$\left[-\frac{\hbar}{2m_e}\nabla^2 + V(r)\right] u(\mathbf{r}) = Eu(\mathbf{r}) \tag{2.12}$$

where E and $u(\mathbf{r})$ are the electron energy eigenvalue and the wave function, respectively. The wave function can be separated into the radial and the angular parts by substituting

$$u(\mathbf{r}) = R_{nl}(r)Y_{nl}(\theta, \phi) = \frac{\chi_{nl}(r)}{r}Y_{ln}(\theta, \phi)$$

into Eq. (2.12), where $Y_{ln}(\theta, \phi)$ is the spherical harmonics and $\chi_{nl}(r)$ is given by the equation

$$\frac{d^2\chi_{nl}(r)}{dr^2} + k_{nl}(r)^2\chi_{nl}(r) = 0,$$
$$k_{nl}(r)^2 = \frac{2m_e}{\hbar^2}\left[E - \frac{l(l+1)\hbar^2}{2m_e r}V(r)\right]$$

where $l = 0, 1, 2, \cdots, n-1$. $V(r)$ is usually expressed as a sum of the potential screened by bound electrons and the effective potential due to the electron-electron correlation:

$$V(r) = V_0(r) + V_{\text{exc}}(r).$$

$V_0(r)$ is given by the Poisson equation

$$\nabla^2 V_0(r) = -4\pi e^2 \left[Z\delta(r) - \rho(r)\right]$$

where δ is the Delta function, and $\rho(r)$ is defined by

$$\rho(r) = \frac{1}{4\pi r^2}\sum_{nl} P_{nl}.$$

$\chi_{nl}(r)$ is normalized to be

$$\int_0^\infty \chi_{nl}(r)^2\, dr = 1.$$

For the effective potential due to the electron-electron correlation, the local approximation by Slater

$$V_{\rm exc} = -\left(\frac{24}{\pi}\rho(r)\right)^{1/3} \qquad \text{(Ry)}$$

is used. When the wave functions are obtained, the dipole oscillator strength[29] can be obtained by

$$f_{n'l',nl} = \frac{1}{3}\frac{\max(l,\, l')}{2l+1}\frac{\nu_{n'l'}^{nl}}{\rm Ry}\frac{\left(R_{nl}^{n'l'}\right)^2}{{a_0}^2}$$

where $\nu_{n'l'}^{nl}$ is the frequency of the transition $nl - n'l'$, Ry is the Rydberg constant, and the radial integral (dipole moment) $R_{nl}^{n'l'}$ is defined by

$$R_{nl}^{n'l'} = \int_0^\infty R_{n'l'} r R_{nl}\, r^2 dr.$$

Using the HFS model, we have calculated the electron energy level and the absorption oscillator strength of the gold ions, of which levels up to 3 are fully occupied by bound electrons. Dependence on a number of bound electrons for $4p-4d$ and $4d-4f$ transitions is shown in Fig. 2.17, while dependence for $4p-5d$, $4d-5f$, and $4f-5g$ transitions is shown in Fig. 2.18.

The oscillator strength is shown in (a), while the transition energy is shown in (b). In (a)'s of Figs. 2.17 and 2.18, the broken lines are the oscillator strength used in the atomic model explained in Sec. 2.3, which does not depend on a number of bound electrons in the level of $n = 4$. The values are those of the Cu-like ($1s^2 2s^2 2p^6 3s^2 3p^6 3d^{10}$ + one electron) gold ions which are the results by the MCDF code. In the MCDF code, the relativistic effect and the effect of the configuration interaction using the wave function of the one electron approximation are taken into account. The data in the case of Cu-like ion are much more accurate than that by the simple HFS model. The difference between results of the MCDF code and the HFS model in the Cu-like ion is estimated to be at most about 20 %. As a number of electrons in the level of $n = 4$ increases, the oscillator strength of $n = 4 - 5$ decreases, while the oscillator strength between sublevels of $n = 4$ increases. From the figure, errors in the oscillator strength used in Sec. 2.3 are estimated at most about a factor of 2 to those of the level of $n = 4$.

In (b)'s in Figs. 2.17 and 2.18, the broken lines are the transition energy of the SHM including l-splitting, while the solid lines are the corresponding HFS results. As a number of bound electrons in the level of $n = 4$ increases, the transition energy from the level of $n = 4$ to the level of $n = 5$ decreases, while the transition energy between the sublevels of $n = 4$ increases. The SHM including the l-splitting support the tendency and the deviation from the HFS results are at most less than 15 % to those of the level of $n = 4$.

2.5.2 j-splitting in the electron energy level

The importance of the j-splitting in the energy level structure of the high-Z ions like gold is first shown by Finkenthal[26]. Table 2.3 shows the detailed transition energy and oscillator strength by the RELAC code[23]. The RELAC code can give a parametric

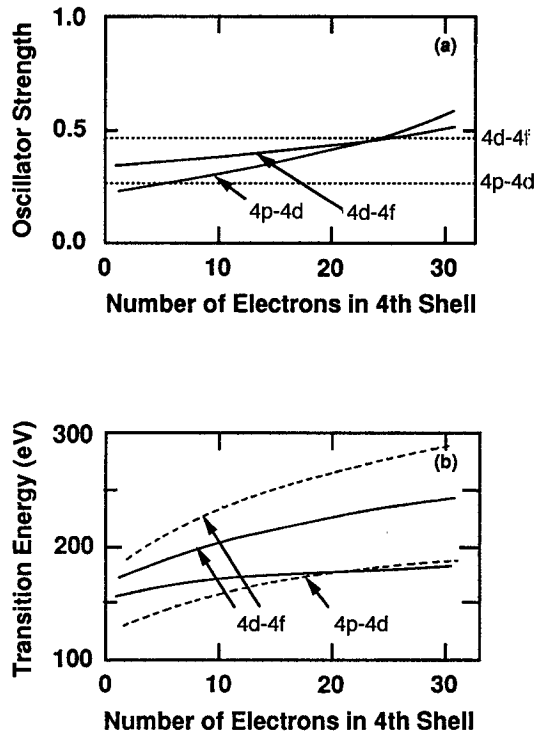

Figure 2.17: Transition energy and absorption oscillator strength of the $4p - 4d$ and $4d - 4f$ transitions of the gold ions. (a) Oscillator strength. (b) Transition energy. Solid lines are results by Hartree-Fock-Slater model, while the broken lines are those used in this thesis.

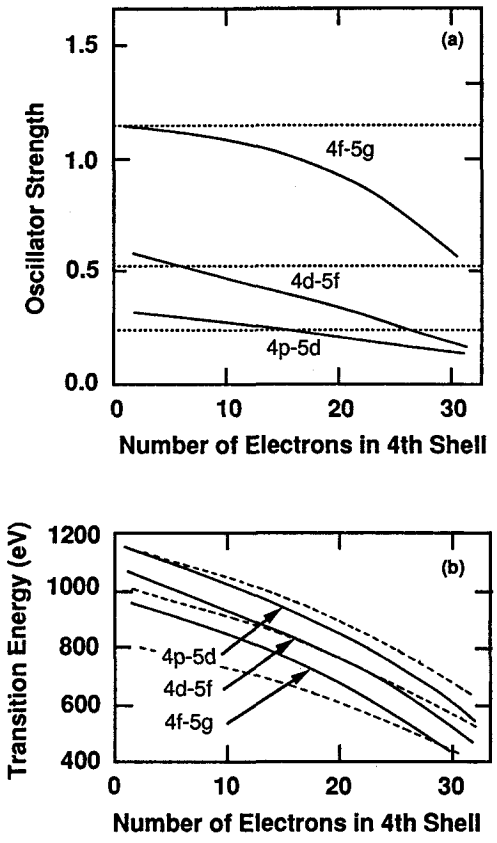

Figure 2.18: Transition energy and absorption oscillator strength of the $4p-5d$, $4d-5f$, $4f-5g$ transitions of the gold ions. (a) Oscillator strength. (b) Transition energy. Solid lines are results by Hartree-Fock-Slater model, while the broken lines are those used in this thesis.

potential for the given electronic configuration of the ion. Using the potential, we can calculate detailed ab initio energy levels. Compared with the RELAC calculation, the transition energy of $4d - 4f$ obtained by the SHM does not differ substantially. But the transition energy of $4p - 4d$ by the RELAC code splits into two line group, i.e., at about 33 Å for $4p_{1/2} - 4d$ and at about 50 Å for $4p_{3/2} - 4d$. The line group of the lower energy corresponds to transition given by the SHM, but the line group of which energy is higher than that of $4d - 4f$ is purely j-splitting effect.

Table 2.3: RELAC calculations for $4d - 4f$ and $4p - 4d$ transitions of RbI-like ions

Transition	$J - J$	Au^{42+}		Pb^{45+}	
		λ_m (Å)	gf	λ_m (Å)	gf
$4p^6 4d - 4p^6 4f$	$3/2 - 5/2$	49.28	4.01	45.52	4.26
	$5/2 - 5/2$	55.23	0.23	51.86	0.06
	$3/2 - 7/2$	54.00	3.43	50.22	3.58
$4p^6 4d - 4p^5{}_{1/2} 4d^2$	$3/2 - 1/2$	37.93	1.21	33.67	1.14
	$3/2 - 3/2$	37.05	3.89	33.11	3.25
	$3/2 - 5/2$	40.35	2.08	35.75	1.72
	$5/2 - 3/2$	37.65	2.91	33.44	2.90
	$5/2 - 5/2$	37.95	5.21	33.73	4.85
	$5/2 - 7/2$	38.08	3.30	33.68	4.96
$4p^6 4d - 4p^5{}_{3/2} 4d^2$	$3/2 - 3/2$	55.72	1.50	51.32	1.60
	$5/2 - 3/2$	54.43	1.84	50.22	1.90
	$5/2 - 5/2$	54.02	3.11	49.85	3.40

In the experiment of the Pb, the two-peaked structure of the X-ray is observed. Figure 2.19 shows the time-integrated X-ray spectra where the experimental spectrum is shown by the solid line, while the numerical one is by the broken line. The irradiated laser intensity is 2×10^{14} W/cm^2. This condition is not so different from that of Figs. 2.15 and 2.16, but the 100-μm-diameter spot size is 10 times smaller. We may guess that the local temperatures in the plasma may be higher than that in the experiment shown in Fig. 2.15, in which relatively uniform plasma is produced due to the large laser energy. By the simulation, the X-ray conversion rate can be perfectly reproduced, but the two-peaked structure seen in the experiment can not. From Table 2.3, the two-peaked structure in the X-ray spectrum is due to the $4d - 4f$ and $4p_{1/2} - 4d$ transitions for the line group at about $300 \sim 320$eV and the $4p_{3/2} - 4d$ transitions for the line group at about $340 - 380$eV.

2.5.3 Validity of statistical model

Using the statistical model, we can calculate the population for each charge state from the fractional population of the average ion model. In order to show the accuracy of the statistical method, we compare the results with those by the detailed configuration accounting (DCA) model[30]. In the DCA model, the rate equation for each charge state is solved separately. Figure 2.20 shows the ionic distribution of each charge state in the aluminum plasmas of which ion density are 10^{20} cm^{-3} in the CRE model. The solid lines are the ionic distribution of each charge state obtained from the fractional population

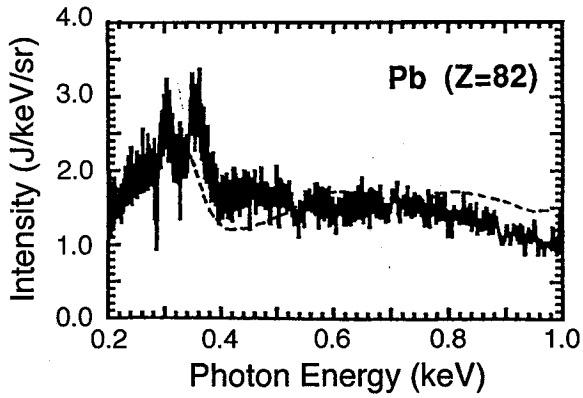

Figure 2.19: Time-integrated X-ray spectra by the laser irradiation of 2×10^{14} W/cm^2 where the experimental spectrum is shown by the solid line and the numerical one by the broken line. The laser condition is not so different from that of Fig. 2.15, but the spot size of 100 μm in diameter is 10 times smaller. The numerical simulation can not reproduce the two-peaked structure at about 300 $\sim$ 400eV.

of the average ion model, while the dashed lines are those by the DCA model. The numbers in the figure show the charge states. Although it also shows a small shift of the distribution of the charge state to the lower temperature side, the distribution can be well reproduced even in the case of low-Z plasma.

Next, we show the population calculated by the statistical model lead to the Saha equilibrium in the LTE limit. $F_{P_n=k}$ is assumed to be the probability of finding k bound electrons in the level n. The ratio of the probability of finding k and $k+1$ bound electrons is given by

$$\frac{F_{P_n=k}}{F_{P_n=k+1}} = \left(\begin{array}{c} D_n \\ k \end{array} \right) \Big/ \left(\begin{array}{c} D_n \\ k+1 \end{array} \right) \times \frac{1-x_n}{x_n}$$

where $x_n = P_n/D_n$ and

$$\left(\begin{array}{c} D_n \\ k \end{array} \right) = \frac{D_n!}{(D_n-k)!k!}.$$

In the LTE,

$$\frac{1-x_n}{x_n} = \exp\left(\frac{E_n-\mu}{k_{\rm B}T_{\rm e}}\right)$$

is derived because x_n is the Fermi-Dirac distribution. If the change in E_n and μ is small enough when a number of bound electrons in the level changes, the fraction p_k becomes that of the Saha equilibrium. The assumption is used in the average ion model, so that the population by the statistical method becomes that of the Saha equilibrium in the LTE limit.

2.5.4 Comparisons with the results of detailed opacity codes

The opacity workshop: WorkOp is held every 3 years. The opacity code based on the model shown in this section was submitted to the comparison study twice in 1994 and 1997. In this subsection, the typical results and a difference from results by the other detailed opacity codes are briefly shown[31, 32]. In the WorkOp:94, the opacities in the

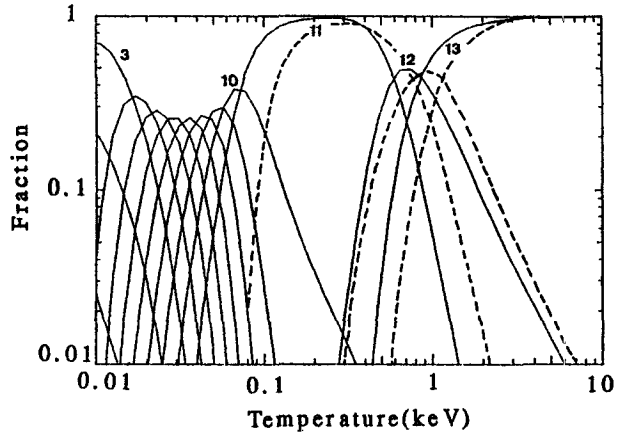

Figure 2.20: Ionic distribution of each charge state in the aluminum plasmas of which ion density are 10^{20} cm^{-3} in the CRE model. The solid lines are the ionic distribution of each charge state obtained from the fractional population of the average ion model, while the dashed lines are those by the DCA model. The numbers in the figure show the charge states. Although it also shows a small shift of the distribution of the charge state to the lower temperature side, the distribution can be well reproduced even in the case of low-Z plasma.

CRE are also discussed. From the WorkOp:97, the objective was limited to the opacity in the LTE.

More than ten opacity codes had been submitted. For the atomic model, the average ion model or the detailed configuration accounting model is used. For the energy levels, the simple SHM including the l-splitting or a solution to the Schrödinger or Dirac equation within the one electron approximation, using either the parametric potential or the self-consistent field is used.

The code we have submitted is based on the average ion model and the SHM including the l-splitting. The code is named "CORONA". In the code, the population for different charge states is calculated by the statistical model shown in Sec. 2.4. In the process, excited states among sublevels of the same principal quantum number are also taken into account. The level of $n = 3$ for example, $2 \times 6 \times 10$ states are taken into account for the electronic configuration. In calculating the detailed spectral opacity, the line profile becomes much more important. In the code, the natural broadening due to the lifetime of the level, the Doppler broadening due to the ion motion, and the electron collisional broadening shown by Griem[33] are taken into account. In the model, the (angular frequency) width of a line, i.e. one half its damping constant, becomes

$$w = 8\left(\frac{\pi}{3}\right)^{3/2}\frac{\hbar a_0}{m_e}N_e\left(\frac{\mathrm{Ry}}{k_B T_e}\right)^{1/2}\left[\left\langle i\left|\frac{r^2}{{a_0}^2}\right|i\right\rangle g\left(\frac{3k_B T_e}{2\Delta E_i}\right)+\left\langle f\left|\frac{r^2}{{a_0}^2}\right|f\right\rangle g\left(\frac{3k_B T_e}{2\Delta E_f}\right)\right]$$

where

$$\left\langle k\left|\frac{r^2}{{a_0}^2}\right|k\right\rangle \sim \frac{1}{2}\left(\frac{n_k}{Z}\right)^2[5{n_k}^2+1-3l_k(l_k+1)].$$

In this equation, i and f means the initial state and final state.

First, the case of the hydrogen is shown in Fig. 2.21, where the electron temperature is 1 eV and the density 1×10^{-6} g/cm^3. The hydrogen is not high-Z treated in this

chapter, but the model for hydrogen is of fundamental for other cases. The average ionization degree by the CORONA is about 0.012, while the results by detailed codes are $0.077 \sim 0.078$. The difference is due to the atomic modeling. In the CORONA, the Fermi-Dirac distribution in the average ion model is used while the Saha-Boltzmann distribution is used in the detailed codes. For hydrogenic ions, the Fermi-Dirac distribution can not give the correct ionization degree. The Planck and Rosseland mean opacities by the CORONA are about $6.0 \times 10^4 \mathrm{cm}^2/\mathrm{g}$ and about $7.2 \times 10^5 \mathrm{cm}^2/\mathrm{g}$, while those by detailed codes are $1.6 \sim 1.7 \times 10^5 \mathrm{cm}^2/\mathrm{g}$ and $4.4 \sim 4.6 \times 10^5 \mathrm{cm}^2/\mathrm{g}$. The difference in the Planck mean opacity is due to the modeling on the free-free process. The detailed treatment of the Gaunt factor for the free-free process is required. In the results by detailed codes, bound-free edge of the M-shell can not be seen. The difference in the Rosseland mean opacity is due to the modeling of the bound-bound spectral profile. In the detailed codes, the microfield in the plasma is calculated. As other problem in the CORONA, we quote that the series limits of the bound-bound transition do not merge into bound-free edge even though the states up to $n = 100$ are taken into account. The corresponding experimental results can be found in Ref. [34]

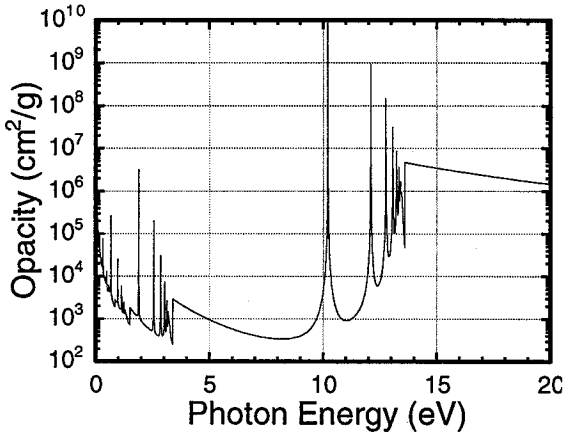

Figure 2.21: Hydrogen plasma opacity where the electron temperature is 1 eV and the density 1×10^{-6} g/cm^3.

Figure 2.22 shows the opacity of the carbon where the electron temperature is 20 eV and the density 10 g/cm^3. The carbon is also not high-Z treated in this chapter, but this case shows the importance of treating the free states. The average ionization degree by the CORONA is about 3.5, and the Planck and Rosseland mean opacities by the CORONA are about $6.0 \times 10^4 \mathrm{cm}^2/\mathrm{g}$ and about $7.2 \times 10^5 \mathrm{cm}^2/\mathrm{g}$, while we couldn't obtain the consensus for the parameters among the detailed codes. In Fig. 2.22, the K-edge of the H-like carbon can be seen at about 275 eV, but the structure becomes dull because the continuum state near ionization threshold is almost occupied by free electrons. This treatment for the free states can be easily installed into the average ion model. The treatment is delicate. As a conclusion, we need experimental data to be compared with theoretical calculations. The numerical value of this opacity may be important for the inertial confinement fusion research.

Table 2.4 shows the density dependence of the mean opacities of iron plasmas. The upper values are results by the CORONA, while the lower values are results by detailed opacity codes. The average ionization degree $Z_e \sim 8.6$ are almost the same for all cases.

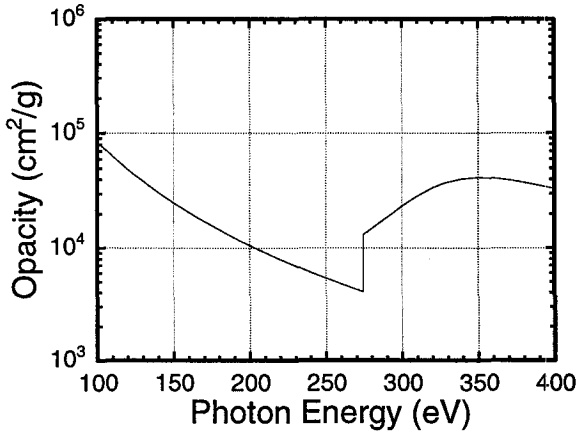

Figure 2.22: Carbon plasma opacity where the electron temperature is 20 eV and density 10 g/cm^3.

The line spectra which contribute the resultant opacity are those of ions with $17 \sim 18$ bound electrons (Cl-like and Ar-like). Under this condition, the contribution of the term-splitting becomes important. This effect is enhanced in the low density. From Table 2.4, as the plasma density increases, the difference between the results by the CORONA and the detailed opacity codes decreases. For the dense plasma more than 0.01g/cm^3, the line broadening due to the electron collisional process becomes significant, so that the term-splitting effect relatively reduced. As it seldom occurs that the plasmas of which density is less than 10^{-2}g/cm^2 becomes important in the usual laser produced plasma, we can conclude the opacity data by the CORONA is good enough for the simulation of the laser produced plasmas.

Table 2.4: Density dependence of the mean opacities of iron plasmas. The upper values are results by the CORONA, while the lower values are by the detailed opacity codes.

Condition	χ_P(cm^2/g)	χ_R(cm^2/g)
16.35 (eV), 10^{-5} (g/cm^3)	7.8×10^3	9.5×10^1
	$(3 \sim 4 \times 10^4)$	$(1 \sim 3 \times 10^3)$
20 (eV), 10^{-5} (g/cm^3)	9.1×10^3	8.6×10^2
	$(3 \sim 4 \times 10^4)$	$(6 \sim 8 \times 10^4)$
24.63 (eV), 10^{-5} (g/cm^3)	1.2×10^4	3.9×10^3
	$(3 \sim 4 \times 10^4)$	$(1 \sim 2 \times 10^4)$
31.70 (eV), 10^{-5} (g/cm^3)	1.4×10^4	9.0×10^3
	$(3 \sim 4 \times 10^4)$	$(3 \sim 4 \times 10^4)$

In Figs. 2.23 and 2.24, the opacity calculated by the CORONA is compared with the corresponding transmission measurement. The transmission is defined by

$$T = \exp(-\chi\rho d)$$

where χ, ρ, and d are the opacity, the density of the plasma, the thickness of the plasma, respectively. The solid line is the result by the CORONA and the thin line is the experimental one.

Figure 2.23 shows the case where the density is $0.01 g/cm^3$ and the temperature 20eV. The corresponding mean opacity is shown in Table 2.4. The detail of the experiment can be found in Ref. [35]. The M-edge structure of iron plasma is seen in. Though the three-peaked structure by the CORONA is shifted to the lower energy side by about 25 eV, the global structure of the spectrum is well reproduced. Determining the position of three-peaks which is related to the accuracy of the energy level calculation is also difficult for other detailed opacity codes, since the effect of the spin-orbit interaction becomes important in this three-peaked structure.

Figure 2.24 shows the case where the density is $0.0113 g/cm^3$ and the temperature 59eV. The detail of the experiment can be found in Ref. [36]. The L-edge structure of iron plasma is seen in, and the CORONA can well reproduce the experimental result, since the SHM can calculate the values of the electron energy level of $n = 2$ accurately, compared with those of the level of $n = 3$.

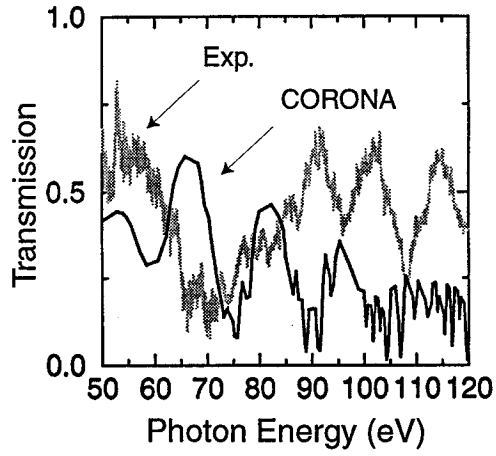

Figure 2.23: The opacity calculated by the CORONA are compared with the corresponding transmission measurement, where the density is $0.01 g/cm^3$ and the temperature 20eV. The solid line is the result by the CORONA and the thin line is the experimental one. M-edge structure can be seen in the figure.

2.6 Summary

We have summarized atomic models that have been used in the hydrodynamic codes of the inertial confinement fusion research, i.e., the screened hydrogenic model (SHM), the detail of the rate coefficients, the model for the pressure ionization and the continuum lowering, the collisional radiative equilibrium (CRE) model and the local thermodynamic equilibrium (LTE) model, and the detail of formulae of the emissivity and opacity calculations.

In Sec. 2.3, we have shown a new model for calculating the spectral opacity and emissivity of high-Z plasma like gold for solving the X-ray transport in hydrodynamic codes. In the model, plasmas are assumed in the CRE. The l-splitting effect, i.e., the consideration of the azimuthal quantum number in the electron energy levels is introduced using the SHM developed by Perrot. As a result of a gold plasma, the electron energy level E_4 of Au^{+40}, for example, splits into four sublevels with the width of about 300 eV

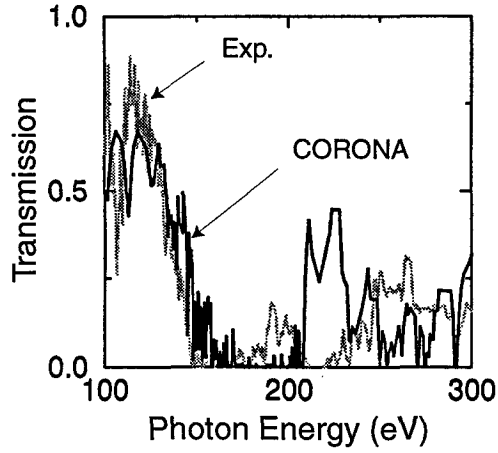

Figure 2.24: The opacity calculated by the CORONA is compared with the corresponding transmission measurement, where the density is 0.0113g/cm^3 and the temperature 59eV. The solid line is the result by the CORONA and the thin line is the experimental one. L-edge structure can be seen in the figure.

by including the l-splitting effect. The transitions between the sublevels, such as $4d-4f$, are important elements to understand the strong peak near 200 eV in the experimental spectra of gold plasmas.

In Sec. 2.4, we have shown a line profile modeling for the average ion model. For the opacity and emissivity of the partially ionized high-Z plasmas like gold, the line profile is approximated to be the Gaussian profile of which width is determined by the ionic distribution of different charge states. This opacity and emissivity are installed into the hydrodynamic code ILESTA-1D to examine the experimental spectra. As a result of the simulation, the peaked X-ray near 200 eV seen in the experiment stems from the lines due to the $\Delta n = 0$ transition between the sublevels of $n = 4$. In addition, relatively flat spectra in $h\nu = 400 \sim 800$ eV seen in the experiment can be explained as a result of the l-splitting of the line of the $4-5$ transition. The line group of the $4f-5g$, $4d-5f$, and $4p-5d$ transitions mainly forms this flat structure.

In the simulation of the X-ray generation by laser produced plasmas like gold, the assumptions that the plasmas are in the CRE, the l-splitting effect, and the line profile modeling if the average ion model is used, are essentially important to reproduce the global structure of the X-ray spectrum of the corresponding experiment.

In Sec. 2.5, we have examined the accuracy of this atomic model for the opacity and emissivity calculation of the high-Z plasmas in detail.

We have compared the values of the electron energy level and oscillator strength with the values by the Hartree-Fock-Slater (HFS) model. From the HFS results, as a number of electrons in the level of $n = 4$ increases, the oscillator strength of $n = 4-5$ decreases, while the oscillator strength between sublevels of $n = 4$ increases. Errors in the oscillator strength used in Sec. 2.3 are estimated at most about a factor of 2 to those of the level of $n = 4$.

We have discussed the j-splitting effect briefly. For the high-Z ions like gold, the transition energy of the $4d-4f$ obtained by the SHM with l-splitting does not differ substantially from the detailed theoretical value including the spin orbit interaction. The transition energy of the $4p-4d$, however, split into two line group, i.e., at about 33 Å

for $4p_{1/2} - 4d$ and at about 50 Å for $4p_{3/2} - 4d$. The line group of the lower energy corresponds to transition given by the SHM, but the the line group of which energy is higher than that of $4d - 4f$ is purely j-splitting effect. The two-splitted structure of the soft X-ray region is actually observed in the experiment of the Pb. Inclusion of the j-splitting effect would be a next subject in future.

We have shown the accuracy of the population for each charge state that is calculated from the fractional population of the average ion model by the comparison with those obtained by the detailed configuration accounting (DCA) model on the aluminum plasmas. In the DCA model, the rate equation for each charge state is solved separately. Although it also shows a small shift of the distribution of the charge state to the lower temperature side, the distribution can be well reproduced even in the case of low-Z plasma.

Finally, we have shown the comparison study between the spectral opacity based on the model developed in this chapter and the results by detailed opacity codes for the case of hydrogen, carbon, and iron plasmas.

For the low density and low discharged hydrogen plasma, it is difficult to estimate the correct average ionization degrees with the average ion model.

In the case of the dense carbon plasma of which density is more than the solid density, the continuum state near ionization threshold is almost occupied by free electrons. This treatment for the free states can be easily installed into the average ion model. But there are no reliable experimental results of such extreme condition that can be compared with the theoretical results.

From the density dependence of the mean opacity of iron plasmas, we have obtained the applicable density limit of the present model. In the case of low density less than $0.01\mathrm{g/cm}^3$, the contribution of the term-splitting becomes important. As it seldom occurs that the plasmas of such density becomes important in the usual laser produced plasma, we can conclude the opacity data by the CORONA is good enough for the simulation of the laser produced plasmas.

For the energy level related to the L shell ($n = 2$), the SHM can give accurate values which can be compared with the experimental ones, while for the energy level related to the M shell ($n = 3$), the SHM can not give accurate values enough. Determining the energy level related to the M shell is also difficult for other detailed opacity codes, since the effect of the spin-orbit interaction becomes important.

References

[1] R. Kodama, K. Okada, N. Ikeda, M. Mineo, K. A. Tanaka, T. Mochizuki, and C. Yamanaka, J. Appl. Phys. **59**, 3050 (1986).

[2] 高部英明, 三間圀興, 核融合研究 68 別冊, 13 (1992).

[3] P. D. Goldstone, S. R. Goldman, W. C. Mead, J. A. Cobble, G. Stradling, R. H. Day, A. Hauer, M. C. Richardson, R. S. Marjoribanks, P. A. Jaanimagi, R. L. Keck, F. J. Marshall, W. Seka, O. Barnouin, B. Yaakobi, and S. A. Letzring, Phys. Rev. Lett. **59**, 56 (1987).

[4] H. Nishimura, H. Takabe, K. Kondo, T. Endo, H. Shiraga, K. Sugimoto, T. Nishikawa, Y. Kato, and S. Nakai, Phys. Rev. A **43**, 3073 (1991).

[5] H. Mayer, Los Alamos Scientific Laboratory Report, LA-647, 1947.

[6] W. A. Lokke, and W. H. Grasberger, Lawrence Livermore National Laboratory Report No. UCRL-52276, 1977

[7] R. D. Cowan, *The theory of atomic structure and spectra* (University of California Press, Berkeley, 1981), p. 194.

[8] R. M. More, J. Quant. Spectrosc. Radiat. Transfer **27**, 345 (1982).

[9] D. Salzmann, and A. Krumbein, J. Appl. Phys. **49**, 3299 (1978).

[10] M. Itoh, T. Yabe, and S. Kiyokawa, Phys. Rev. A **35**, 233 (1987).

[11] H. Takabe, Institute of Laser Engineering Research Report No. ILE9008P, 1990 (unpublished).

[12] H. A. Bethe, and E. E. Salpeter, *Quantum Mechanics of One- and Two-Electron Atoms* (Plenum Publishing, New York, 1977), p. 264.

[13] G. B. Zimmerman, and R. M. More, J. Quant. Spectrosc. Radiat. Transfer **23**, 517 (1980).

[14] K. Takami, (private communication).

[15] M. Busquet, J. Quant. Spectrosc. Radiat. Transfer **43**, 91 (1990).

[16] R. Latter, Phys. Rev. **99**, 1854 (1955).

[17] Ya. B. Zel'dovich, and Yu. Raizer, *Physics of shockwaves and high-temperature hydrodynamic phenomena* (Academic Press, New York, 1966), Chap. IV.

[18] J. Cooper, Rep. Prog. Phys. **29**, 35.

[19] Phys. Scripta **39**, 332 (19899.

[20] H. L. Zhang, D. H. Sampson, and C. J. Fontes, Atom. Data Nucl. Data Tables **44**, 31 (1990).

[21] D. H. Sampson, H. L. Zhang, and C. J. Fontes, Atom. Data Nucl. Data Tables **44**, 209 (1990).

[22] H. L. Zhang, D. H. Sampson, and C. J. Fontes, Atom. Data Nucl. Data Tables **44**, 273 (1990).

[23] K. Murai, M. Nishio, H. Shiraga, Y. Kato, T. Nishikawa, H. Takabe, M. Finkenthal, and P. Mandelbaum, Research Report, Institute of Laser Engineering, Osaka University,

[24] J. Stein, D. Shalitin, and Akica Ron, Phys. Rev. A **31**, 446 (1985).

[25] H. Takabe, and T. Nishikawa, J. Quant. Spectrosc. Radiat. Transfer **51**, 379 (1994).

[26] M. Finkenthal (private communication).

[27] A. Rickert, Max-Planck-Institut für Quantenoptik, MPQ 148, 1989.

[28] A. Rickert, Max-Planck-Institut für Quantenoptik, MPQ 175, 1993.

[29] H. A. Bethe, and E. E. Salpeter, *Quantum Mechanics of One- and Two-Electron Atoms* (Plenum Publishing, New York, 1977), p. 256. 9103p, 1991 (unpublished).

[30] D. Duston and J. Davis, Phys. Rev. A **21**, 1664 (1980).

[31] A. Rickert, K. Eidmann and J. Meyer-ter-Vehn, F. J. D. Serduke, and C. A. Iglesias, Max-Planck-Institut für Quantenoptik, MPQ 204, 1995.

[32] WorkOP 97: Final Report in press.

[33] H. Griem, *Spectral Line Broadening by plasmas*, Academic Press, New York, 1974, p.255.

[34] W. L. Wiese, D. E. Kelleher, and D. R. Paquette, Phys. Rev. A **6**, 1132 (1972).

[35] L. B. Da Silva, B. J. MacGowan, D. R. Kania, B. A. Hammel, C. A. Back, E. Hsieh, R. Doyas, C. A. Iglesias, F. J. Rogers, and R. W. Lee, Phys. Rev. Lett. **69**, 438 (1992).

[36] P. T. Springer, D. J. Fields, B. G. Wilson, J. K. Nash, W. H. Goldstein, C. A. Iglesias, F. J. Rogers, J. K. Swenson, M. H. Chen, A. Bar-Shalom, and R. E. Stewart, Phys. Rev. Lett. **69**, 3735 (1992).

Chapter 3

Atomic models of highly ionized plasmas

3.1 Introduction

In this chapter, treat the atomic model of highly ionized ions. Main applications are line spectra from highly ionized plasmas: for example, line spectra due to the impurity in laser imploded plasmas, and X-ray spectrum from stellar plasmas. If number of bound electron in the open-shell becomes larger than three, or smaller than $(2n^2 - 3)$, number of possible terms of energy levels suddenly increase, so that main objectives are H-like, He-like, and Li-like ions. In the inertial confinement fusion research, spectroscopic measurements of X-ray from imploded plasmas more than solid density have been carried out[2, 3]. Recently, new interest in opacity of stellar plasmas has arisen and precise opacity experiments have been carried out[1]. In order to know density and/or temperature of the plasma, spectroscopic measurements have been widely used in experiment. A lot of detailed experimental results, for example, line profiles has been collected[9, 10]. Even a commercial software for analyzing X-ray spectra from plasmas is also available[11]. Essentially important point in the analysis of X-ray spectra from these plasmas are that precise theoretical modeling and numerical calculations are required for understanding the experimental results. Practically, we need modeling of the plasma effect in atomic processes, atomic data for the elementary processes, calculation of the line profile of each line spectrum or modeling on the line profile for the atomic model, etc.

For energy level and oscillator strength, using a detailed atomic code like the GRASP[7], we can obtain fairly accurate data of isolated ions. Numerical values of experimental data and results of atomic code are also available in literature, for example, Kelly's table[8] and the Opacity Project book by Seaton[9]. However, above-mentioned sets of data are sometimes not enough for building up models of atomic process in the plasmas. From the Grotrian diagram, only data for the dipole allowed transition are available, but the line strength is sometimes strongly affected by the states which are not available. Moreover, we meet a relatively large error in the published data. In this section, we propose new method of energy level data recommendation by screening constant of the screened hydrogenic model.

There are still difficult points for some purposes in treating plasma effects. Among them, we discuss a problem that we always meet when we want to build up a model of atomic process, i.e. cutting off the highly excited states, is discussed and simple estimation for that is shown.

In future, we will integrate opacity code like the case of high-Z plasmas discussed in previous chapter. Since there are a lot of effects we have to study and a lot of work due to the spectroscopic measurement of the plasma density and temperature, we couldn't complete the work.

3.2 Energy level recommendation by screening constant

3.2.1 Introduction

When analyzing spectroscopic data from plasmas, we have to make an appropriate atomic model of the plasma. In the process, we need atomic data of elementary processes, for example, electron energy level, oscillator strength, etc. As for energy level, many authors have published data. They are summarized as theoretical calculations, spectroscopic data, and recommended values. However, the problem is which data we should use for the model. In Table 3.1 are displayed the energy level data for the ground state $1\,^1S_0$ of He-like ions from various authors for example. Usually among the data, systematic differences exist. We have to carefully select the most reliable data from among many published data. This work is called recommendation.

A selection of most reliable data which show a simple atomic number (Z) dependence is one method. The raw numerical values of energy level are not appropriate as an index for data recommendation since their Z^2 dependence is large enough to suppress other Z dependence. The simplest index is a value of the energy level divided by Z^2. In Fig. 3.1, the numerical values in Table 3.1 divided by Z^2 are plotted. All data are almost on the same curve.

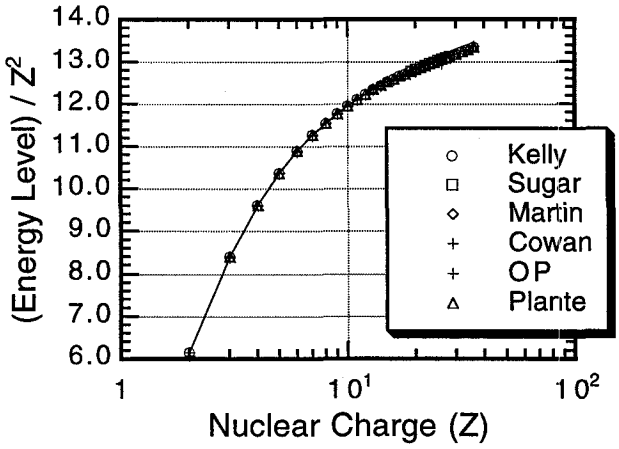

Figure 3.1: Z dependence of the numerical value of energy level divided by Z^2 for the ground state $1\,^1S_0$ of He-like ions. All data are almost on the same curve.

The quantum defect[10] is sometimes used. As the advance of modern computers has enabled us to operate MCDF codes[7], accurate data beyond experimental results are available by numerically for simple ions. However, accurate calculations for complex ions are still difficult, so that the recommendation among the experimental and numerical data is sometimes necessary.

Table 3.1: Energy level data of He-like ground state from various authors. Among the data, systematic differences exist. (Atomic unit)

n	Kelly	Sugar	Martin	Cowan	Opacity Project	Plante
2	0.903557			0.903572	0.893390	
3	2.77968			2.77969	2.76580	2.779961
4	5.65543			5.65545	5.63940	5.655943
5	9.53172			9.53160	9.51350	9.532325
6	14.4087			14.4088	14.3878	14.40974
7	20.2879			20.2896	20.2625	20.28892
8	27.1696			27.1682	27.1371	27.17072
9	35.0549			35.0559	35.0118	35.05615
10	43.9450			43.9475	43.8866	43.94636
11	53.8414			53.8417	53.7610	53.84270
12	64.7455			64.7457	64.6365	64.74663
13	76.6588		76.6588	76.6592	76.5115	76.65982
14	89.5831		89.5799	89.5840	89.3865	89.58405
15	103.521		103.518	103.522		103.5213
16	118.474			118.475	118.137	118.4738
17	134.445			134.446		134.4437
18	151.436			151.438	150.886	151.4337
19	169.448	169.439		169.451		169.4463
20	188.488	188.475		188.491	187.636	188.4845
21	208.559	208.540		208.548		208.5513
22	229.659	229.641		229.656		229.6498
23	251.793	251.775		251.764		251.7835
24	274.966	274.944		274.952		274.9560
25	299.183	299.165		299.184		
26	324.443	324.420		324.416	321.886	324.4326
27	350.760	350.737		350.728		
28	378.125	378.097				378.1125
29	406.551					
30	436.040					436.0310
31	466.598					
32	498.228					498.2284
33	530.937					
34	564.731					564.7469
35	599.605					
36	635.508					635.6334

On the other hand, the screened hydrogenic model (SHM) was first proposed by Slater[11] to calculate non-hydrogenic energy level within the hydrogenic model. In the model, the screening constant represents a reduction factor of the nuclear charge the outer shell electron feels in the presence of the inner electron. Mayer[12] calculated many screening constants, showing the importance of line transitions in the mean opacity calculation of iron plasmas. Since the Mayer's screening constants were based on the hydrogenic wave function, they were not plausible for partially ionized high-Z plasmas. More[13] determined a new set of screening constants, by enormous ionization energy database. Improvement reproducing the hydrogen-like ions and an extension including the l-splitting have been done by Marchand *et al.*[14] and by Perrot[15], respectively.

Since the simple iterative calculation using the SHM and the average ion model[16] gives an electronic population with good accuracy and the emissivity and the opacity could be calculated easily, the SHM's have been widely used in the simulation of inertial confinement fusion. Even the X-ray spectra from high-Z plasmas like gold could be reproduced by hydrodynamic code[17]. Since an accuracy of the resulting opacity and emissivity depends on the screening constants, a new set of the screening constants is required if we need a more accurate result. In the process of obtaining a new set of the screening constants, we have found simple Z dependence of the screening constant. This Z dependence gives not only a simple description of the energy level of ions but is also useful as an index for energy level data recommendation.

In this section, we study the Z dependence of the screening constant of ions, especially of He-like ions, and propose a new usage of the screening constant, i.e. an energy level data recommendation and an interpolation of reliable data using the Z dependence. In Sec. 3.2.2, we compare the Z dependence of the screening constant and of the quantum defect and show that the screening constant is more appropriate than the quantum defect as an index for energy level recommendation. In Sec. 3.2.3, the Z dependence of the screening constant for He-like ions is discussed and its simple fitting formula of the energy level is given for future reference. The Z dependence of other electronic configurations, Li-like, Be-like, and Ne-like ions, is also discussed and the accuracy of the Kelly's data[8] is discussed. In Sec. 3.2.4, we discuss the physical meaning of this simple Z dependence of the screening constant.

3.2.2 Screening constant and quantum defect

In the hydrogenic assumption, an electronic configuration of an ion is expressed by $(P_1, P_2, \cdots, P_k, \cdots)$ where P_k is the number of electrons in the level labeled by k. Using the screening constant $\sum_{k,k'}$, we calculate the screened charge Z_k and the electron energy level E_k of the kth level in atomic units by

$$Z_k = Z - \sum_{k'<k} \sigma_{k,k'} P_{k'} - \sigma_{k,k}(P_k - 1), \tag{3.1}$$

$$E_k = -\frac{{Z_k}^2}{2n(k)^2} \tag{3.2}$$

where Z is the atomic number (nuclear charge) of the ion and $n(k)$ is the principal quantum number of the kth level. Eqs. (3.1) and (3.2) can be applied for the highest level.

Using the Z dependence of $\sigma = \sum_{k'<k} \sigma_{k,k'} P_{k'} + \sigma_{k,k}(P_k - 1)$, we recommend energy level. For He-like ions, the screened charge and the energy level of the kth level are

expressed by

$$Z_k = Z - \sigma_{k,1} \tag{3.3}$$

$$E_k = -\frac{{Z_k}^2}{2n(k)^2} = \frac{(Z-\sigma_{k,1})^2}{2n(k)^2}. \tag{3.4}$$

Energy levels of He-like ions are calculated and experimentally measured by many authors. In this thesis, the famous wave length table by Kelly[8], comprehensive work by Sugar[18] and Martin[19], detailed theoretical calculations by Accad *et al.*[20], comprehensive data collection and recommendation by Seaton group for the Opacity Project[9], and recent relativistic calculations by Plante *et al.*[21] are selected for this recommendation study. The data of Kelly, Sugar, and Martin had been obtained around 1980, so they contain relatively large errors. Accad's calculation for excited states is based on the relativistic theory of α^2 where α is the fine structure constant for Z's up to 10. Plante's one is relativistic all-order many-body calculations including the Breit corrections, which is considered to be the exact value when relative error is discussed for the energy level recommendation study.

Figure 3.2 shows the Z dependence of the screening constant σ for the ground state $1\,{}^1S_0$ of He-like ions. Although the screening constant can be calculated as 0.625 for all ground state of He-like ions from the variation method using the hydrogenic wave function[22], those calculated from the energy level of actual ions have Z dependence. From Fig. 3.2, the data of the Opacity Project are found on the different line. While Kelly's data and Plante's data are only plotted to avoid the complexity of the figure, the other data are almost on the same line of Kelly's and Plante's.

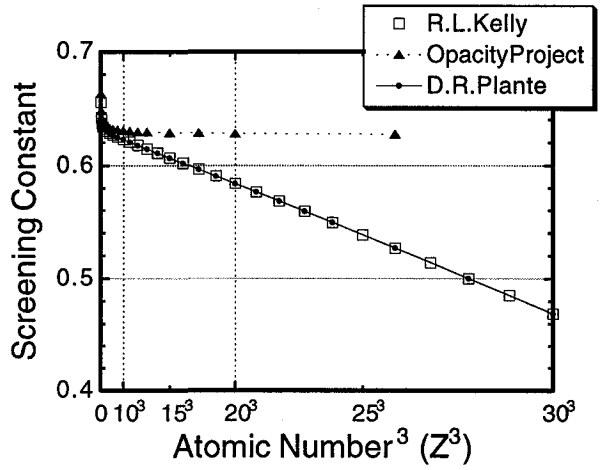

Figure 3.2: Z dependence of the screening constant for the ground state $1\,{}^1S_0$ of He-like ions. Data of the Opacity Project are on the line different from Kelly's and Plante's ones. Simple Z^3 dependence of the screening constant is observed.

On the other hand, the energy level E_k is expressed as

$$E_k = -\frac{(Z-1)^2}{2(n(k)-\epsilon)^2} \tag{3.5}$$

by the quantum defect, and therefore, the quantum defect is calculated to be

$$\epsilon = n(k) - \sqrt{-\frac{(Z-1)^2}{2E_k}}$$

from the energy level. Figure 3.3 shows the Z dependence of the quantum defect. Same data are plotted in both Fig. 3.2 and 3.3, but the appearance is different. Three different data shown by the quantum defect are almost on the same curve and seem to have the same Z dependence.

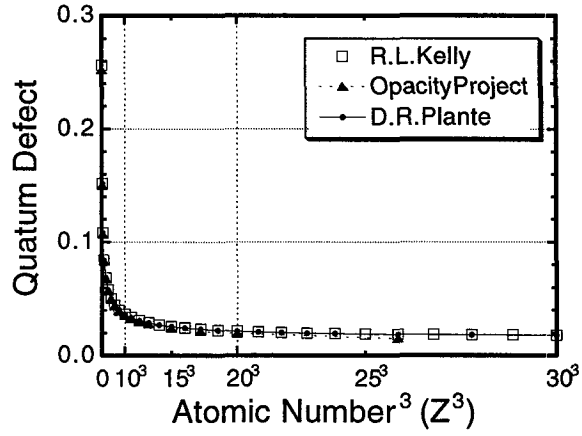

Figure 3.3: Z dependence of the quantum defect for the ground state $1\,^1S_0$ of He-like ions. Compared to Fig. 3.2, three different data are almost on the same curve.

Having been estimated the Z dependence and made extrapolation by the quantum defect, data of the Opacity Project[9] are found on the different line. From the mathematical point of view, the difference in energy level expression between the quantum defect and the screening constant is the subtraction of a constant either from the numerator or from the denominator in the hydrogenic energy level expression $-Z^2/(2n^2)$. From Fig. 3.3, the quantum defect converges to a small value near zero as Z increases. Even in this case, the screening constant monotonously decreases. For high-Z ions, energy level data recommendation by the screening constant is more useful and more accurate than that by the quantum defect.

3.2.3 Atomic number dependence of the screening constant

It is important to note the fact that the screening constant has a clear Z dependence. From Fig. 3.2, the screening constant have the Z dependence as Z^3 for $Z = 10 \sim 40$. Figure 3.4 (a) shows the Z dependence of the screening constant up to $Z = 70$ and (b) shows up to $Z = 100$. From Fig. 3.4, a gradual increase in the power index of Z is found. The Z dependence of the screening constant is approximately Z^3 for $Z = 10 \sim 40$, $Z^{3.5}$ for $Z = 40 \sim 70$, and Z^4 for $Z > 70$.

From Ref. [21], the Breit correction and the QED contribution to the energy level are about 0.3 % of the ionization potential for the ground state of He-like ion of $Z = 70$, for which $\sigma \sim -1.8$ and the energy level calculated by the screening constant is accurate with error less than 0.1 %. Even in the high-Z case, the energy level can be expressed as the simple Z^4 dependence of the screening constant.

Figure 3.5 shows the Z dependence for ions of smaller Z's of $1\,^1S_0$. We also see a slight deviation of the Opacity Project's data from the curve of the most reliable data by Kelly and Plante. For the data of $1\,^1S_0$, the $Z^{-1.5}$ dependence of the screening constant is the best fit. By the dependence, the energy levels of five elements including He atom

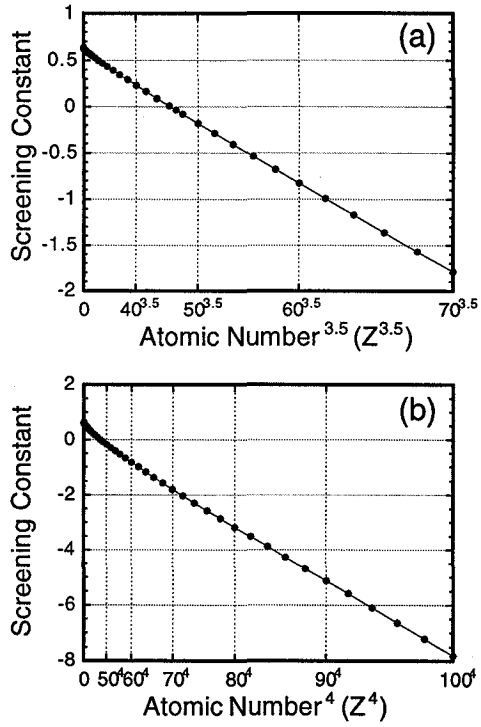

Figure 3.4: Z dependence of the screening constant for the ground state $1\,^1S_0$ of He-like ions of large Z. The Z dependence gradually changes from Z^3 to Z^4. (a) Up to $Z = 70$. (b) Up to $Z = 100$.

can be plotted on the line. However, this dependence changes from level to level. For example, the Z dependence of smaller Z's of He-like $2\,^3P_1$ is shown in Fig. 3.6, where we find clear Z^{-1} dependence.

This monotone Z dependence of the screening constant enables a much more accurate interpolation or extrapolation. Figure 3.7 (a) shows errors in the screening constant by the interpolation. In the process, two ions, Z's of which differ by 4, are used. For reference, the results by the simple linear interpolation are also shown. From Fig. 3.7 (a), absolute values of the interpolation error are always less than 0.01 except some results by the linear interpolation. For high-Z ions, the error by the linear interpolation is usually several times larger than that by the interpolation for which the specific Z dependence is taken into account. The error in the screening constant is the smallest if the interpolation is done, taking into account the Z dependence of Z^3 for $Z = 10 \sim 40$, $Z^{3.5}$ for $Z = 40 \sim 70$, and Z^4 for $Z > 70$. These results correspond to the previously described Z dependence of the screening constant.

Figure 3.7 (b) shows errors of the resulting energy level calculated from the interpolated screening constants. The errors in energy level are usually less than 0.0001 except some cases of larger Z's in the case of the linear interpolation and some cases of $Z = 10$. For ions of which atomic number being around 10, there is no difference between the simple linear interpolation and the interpolation with the assumption of the specific Z dependence of the screening constant. From Eqs. (3.3) and (3.4), the error in energy level is $Z/2$ times smaller than that in the corresponding screening constant. The errors in the screening constant are about 1% for He and about 0.6% for Ne. Therefore, the errors in energy level are about 1% for He and about 0.1% for Ne.

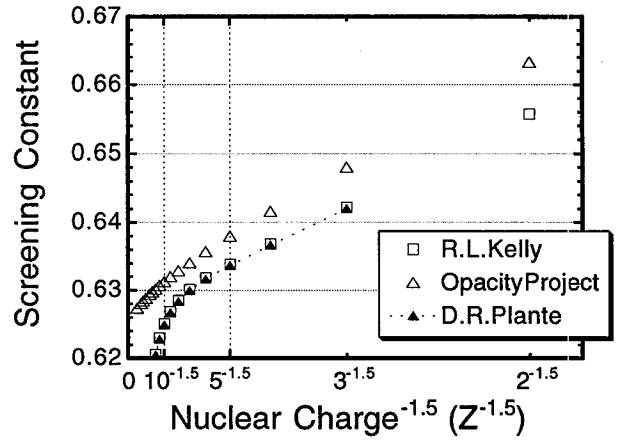

Figure 3.5: Z dependence of the screening constant for the ground state $1\,^1S_0$ of He-like ions of small Z. The screening constant shows the $Z^{-1.5}$ dependence. This dependence changes from level to level.

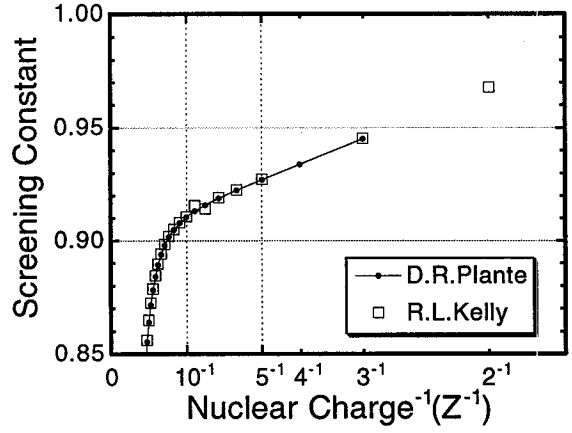

Figure 3.6: Z dependence of the screening constant for $2\,^3P_1$ of He-like ions of small Z. The screening constant shows the Z^{-1} dependence.

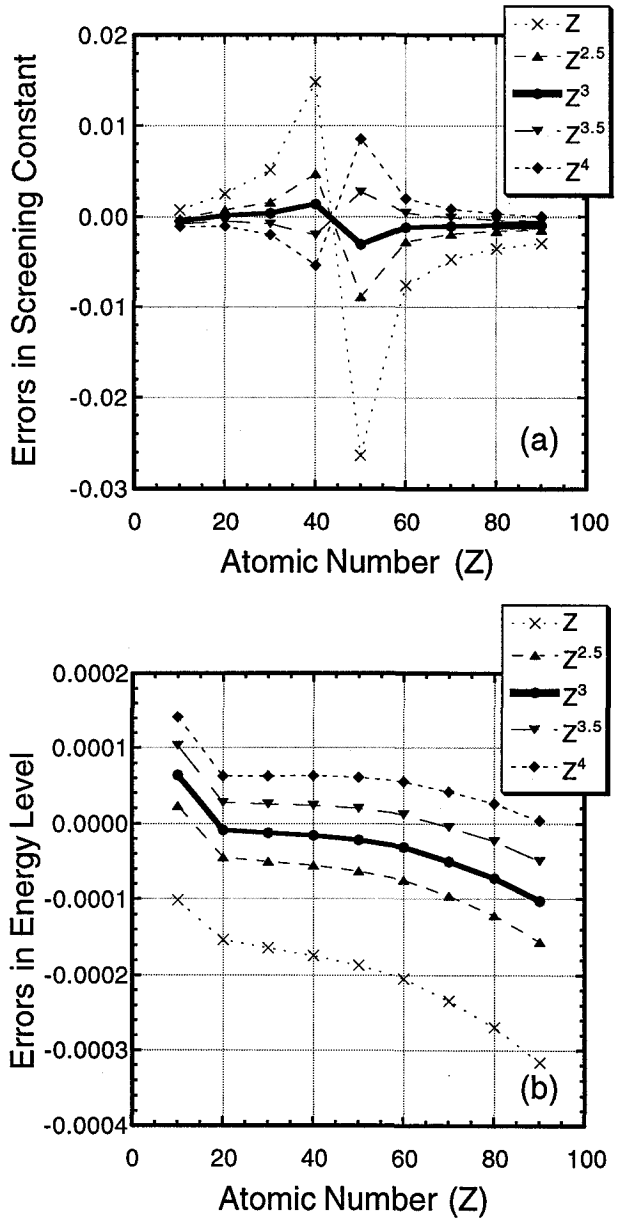

Figure 3.7: Screening constant and resulting energy level by different interpolations are compared for ground state $1\,^1S_0$ of He-like ions. Results using Z, $Z^{2.5}$, Z^3, $Z^{3.5}$, and Z^4 dependence are shown. Values of two ions, Z's of which differ by 4, are used for the interpolations. Error is defined by the difference between Plante's value and that from interpolation divided by the Plante's value. (a) Screening constant. For high-Z ions, error by the linear interpolation is usually several times larger than that by the interpolation for which the specific Z dependence is taken into account. (b) Resulting energy level from the screening constant. Error in energy level is $Z/2$ times smaller than that in the corresponding screening constant.

We see the same Z^3 dependence of σ for different electronic configurations, $2\,^1S_0$, $2\,^1P_1$, $2\,^3S_1$, $2\,^3P_0$, $2\,^3P_1$, and $2\,^3P_2$ for $10 < Z < 40$. However, the dependence of smaller Z's is slightly different in each case. Table 3.2 shows the power index on Z in the Z dependence of the screening constant. We could not find simple Z dependence for ions of smaller Z's of $2\,^1S_0$. The most general power indexes of the Z dependence are Z^{-1} for $Z < 5$, Z^3 for $10 < Z < 40$, and Z^4 for $Z > 70$,

Table 3.2: Power indexes of the Z dependence of the screening constant for He-like ions. The general power indexes are Z^{-1} for $Z < 5$, Z^3 for $10 < Z < 40$, and Z^4 for $Z > 70$.

State	$Z < 10$	$10 < Z < 40$	$Z > 70$
$1\,^1S_0$	-1.5	3	4
$2\,^1S_0$	(-1)	3	4
$2\,^1P_1$	-0.5	2.5	3.5
$2\,^3S_1$	-1.5	3	4
$2\,^3P_0$	-1	3	4
$2\,^3P_1$	-1	3.5	4
$2\,^3P_2$	-1	2.5	3.5

We also see such simple Z^3 dependence for other excited states of He-like ions. Figure 3.8 shows the screening constant for $^1S_0$ up to $n = 5$. As the principal quantum number increases, it becomes hard to obtain reliable data of energy levels. In Fig. 3.8, we see two strange data of $Z = 20$ and 24 in the case of $n = 4$. These data are from Sugar's. As the same feature of a slightly zigzag shape can be seen in the case of $n = 5$ for the same Z's, these data are likely to be obtained either by interpolation or by extrapolation from other reliable ones.

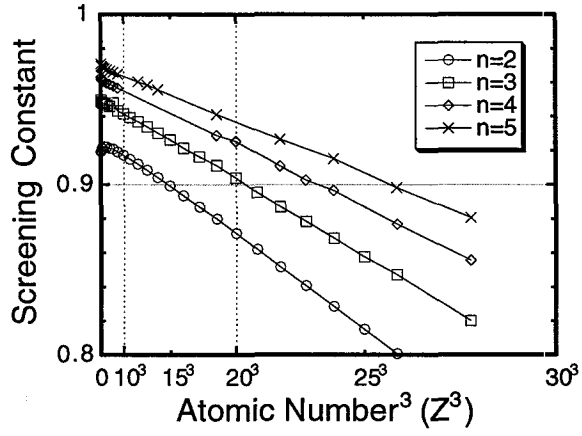

Figure 3.8: Z dependence of the screening constant for $^1S_0$ of He-like ions of $n = 2$, 3, 4, and 5. Two strange data of $Z = 20$ and 24 in $n = 4$ are observed.

Figure 3.9 shows the screening constant for $6\,^1S_0$. As the screening constant has simple Z^3 dependence up to $n = 5$, it would be strange if such simple Z dependence disappears from $n = 6$. Experimental data were usually obtained as transition energy and the accuracy would decrease if the data is expressed as energy level. This may be

one reason we could not see simple Z dependence in published data. The data of highly excited levels with n larger than 5 are also important for practical purpose, because the recombination rate and ionization rate via highly excited states are important, for example, in calculating the total rates by the collisional radiative model[23]. Making reliable data for the levels will be a future study but it would be possible by the simple n dependence of the screening constant.

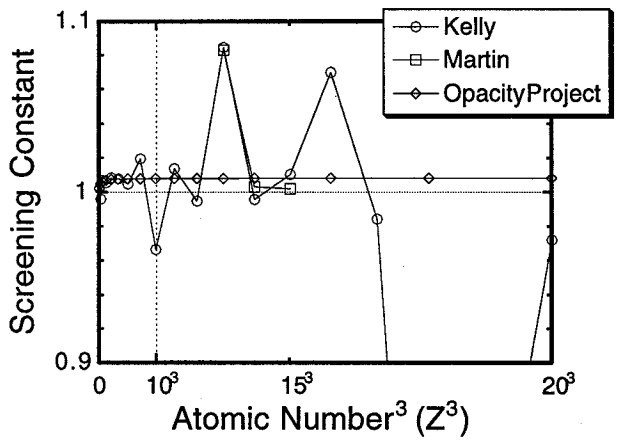

Figure 3.9: Z dependence of the screening constant for $6\,{}^1S_0$ of He-like ions. The data of Kelly, Opacity Project, and Martin are shown. No simple Z dependence is found from published data. As the screening constant has a simple Z^3 dependence up to $n = 5$, it would be strange if such simple Z dependence disappears from $n = 6$.

It is useful for future reference to make a fitting formula in which the above-mentioned Z dependence of the screening constant is taken into account. We define the fitting formula as

$$\sigma(Z) = A + \frac{B}{Z} + C\,Z^3 + D\,Z^4. \tag{3.6}$$

The Z dependence as Z^{-1}, Z^3 and Z^4 are selected because the fitting formula should be as simple as possible. Its accuracy turns out to be not so different, compared with the case where the detailed Z dependence shown in Table 3.2 are used. Table 3.3 shows the coefficients for $n \leq 5$ of the fitting formula. Coefficients are fitted for $Z = 2 \sim 100$ in the cases of $n = 1$ and 2 and for $Z = 2 \sim 28$ in the cases of $3 \leq n \leq 5$, because many data enough for determining the coefficients are not available. In the case of $3 \leq n \leq 5$, the fitting procedure has been done by setting D to zero. By the fitting formula using only 4 fitting parameters, the energy level of ground state for all He-like ions can be calculated within errors of a few % for He, less than 0.7 % for $Z \leq 10$, less than 0.2 % for $Z \leq 20$, and less than 0.1 % for $Z > 20$. For excited levels, errors are much smaller.

Figure 3.10 shows the Z dependence of the screening constant for the ground state of Li-like ions. We see the same simple Z dependence and a slight deviation of the Opacity Project's data from the line of the Kelly's ones.

Figure 3.11 shows the Z dependence of the screening constant for the ground state of Be-like ions. We see the same simple Z dependence up to $Z = 28$. However, the Z dependence of Kelly's data changes from $Z = 29$. We also see this discontinuous feature of Kelly's data for the ground state of B-like, C-like, N-like, O-like, and F-like ions. The error in energy level due to the discontinuity is estimated to be about 0.7 % for the

Table 3.3: Coefficients of the fitting formula Eq. (3.6) of the screening constant for He-like ions. By the fitting formula, the energy level can be calculated with errors of a few % for He atom, less than 0.2 % for $Z > 10$, and less than 0.1 % for $Z > 20$ for the ground state $1\,^1S_0$. For excited levels, errors are much smaller

State	A	B	C ($\times 10^{-6}$)	D ($\times 10^{-8}$)
$1\,^1S_0$	0.60235	0.14475	−3.7661	−4.5829
$2\,^1S_0$	0.89629	0.14475	−4.6833	−5.8777
$3\,^1S_0$	0.95175	−0.0094002	−5.9158	
$4\,^1S_0$	0.96283	−0.0019478	−4.8696	
$5\,^1S_0$	0.96948	0.0018069	−4.0580	
$2\,^1P_1$	1.0217	−0.010643	−1.6037	−0.061952
$3\,^1P_1$	1.0167	−0.054228	−2.5306	
$4\,^1P_1$	1.0121	−0.038371	−2.3249	
$5\,^1P_1$	1.0097	−0.030917	−2.0685	
$2\,^3S_1$	0.74822	0.13025	−6.7655	−3.7628
$3\,^3S_1$	0.84991	0.16137	−6.3903	
$4\,^3S_1$	0.89014	0.12183	−5.1827	
$5\,^3S_1$	0.91366	0.094767	−4.2989	
$2\,^3P_0$	0.87102	0.25573	−4.4113	−6.1519
$3\,^3P_0$	0.94689	0.12920	−5.8933	
$4\,^3P_0$	0.96060	0.094481	−4.7643	
$5\,^3P_0$	0.96854	0.07557	−3.9755	
$2\,^3P_1$	0.88313	0.21127	−4.5429	−6.2528
$3\,^3P_1$	0.94858	0.1171	−5.6097	
$4\,^3P_1$	0.96159	0.087552	−4.5165	
$5\,^3P_1$	0.96936	0.069957	−3.7825	
$2\,^3P_2$	0.90350	0.12518	−1.4139	−0.26904
$3\,^3P_2$	0.94449	0.14386	−2.1156	
$4\,^3P_2$	0.95881	0.10535	−1.9209	
$5\,^3P_2$	0.96717	0.083903	−1.6985	

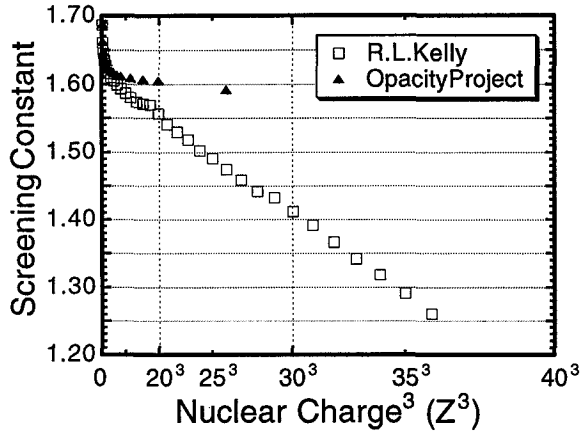

Figure 3.10: Z dependence of the screening constant for the ground state of Li-like ions of Kelly's and Opacity Project are shown. The simple Z^3 dependence is observed. The data of the Opacity Project are on the curve different from those of Kelly's.

ground state of $Z = 29$ ion if the simple Z^3 dependence is adopted. We have to take attention about the discontinuity of the Kelly's energy level data.

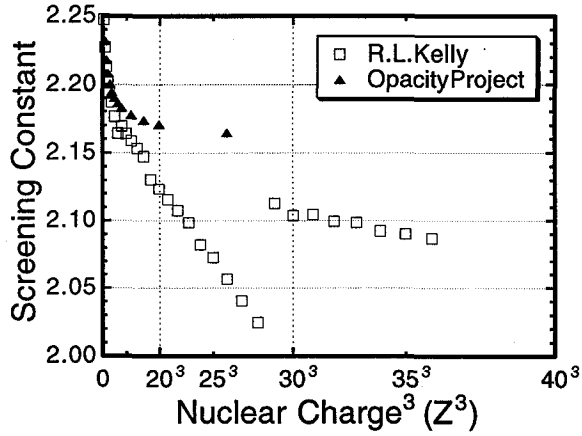

Figure 3.11: Z dependence of the screening constant for the ground state of Be-like ions. Though the Z^3 dependence is observed, Kelly's data of $Z \geq 29$ are on the different line. As the screening constant has the simple Z^3 dependence, the data of $Z \geq 29$ would not be trusted. This tendency in Kelly's data is observed in B-like, C-like, N-like, O-like, and F-like ions, as well.

Figure 3.12 shows the Z dependence of the screening constant for the ground state of Ne-like ions. Here, there is not discontinuous feature at $Z = 29$. Ne-like ions are abundant in plasmas, so relatively accurate data for high-Z ions might be obtained by experiments.

In any case, as a number of bound electron increases, relative value of the screening constant to Z in Eq. 3.4 increases, the energy level data recommendation by the screening constant becomes difficult.

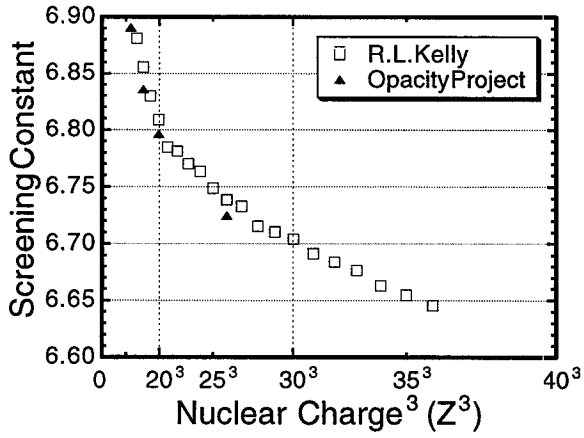

Figure 3.12: Z dependence of the screening constant for ground state of Ne-like ions. The simple Z^3 dependence is observed. Data of the Opacity Project and Kelly are almost on the same curve.

3.2.4 Discussions

As n increases, fitting coefficients vary monotonously. This shows that Eq. (3.6) involves a physical meaning.

To discuss the physical meaning of the Z dependence of the screening constant, it is useful to summarize the screened hydrogenic model (SHM). Here, we quote Perrot's electrostatic expression[15]. In his formulation, the screening constant is defined as related to the interaction energy between two electrons. His hamiltonian for the electronic system is defined by

$$< H >= \sum_n P_n \left(\frac{{Z_n}^2}{2n^2} - \frac{Z Z_n}{n^2} \right) + \sum_n \sum_{n' \leq n} P_n P_{n'} \frac{Z_n}{n^2} \sigma_{n,n'}. \tag{3.7}$$

The first term in the first sum is the kinetic energy and the second term is the interaction energy between nuclear charge Z and the reduced hydrogenic wave function $\Psi(Z_n r)$ where $\Psi(Z_n r)$ is used instead of the hydrogen-like wave function of $\Psi(Zr)$. The second sum is the interaction energy between two electrons expressed by the screening constant $\sigma_{n,n'}$. This equation is different by the factor $(1-\delta_{n,n'}/2)$ from Perrot's original one where $\delta_{n,n'}$ is the Kronecker's δ. While More[13] introduced this factor to satisfy thermodynamic consistency to the plasmas when applying the SHM of which electronic system contains the population $P_n > 1$, the factor is omitted here because there is no difference when the interaction energy between two electrons are discussed. If we use the definition

$$Z_n = Z - \sum_{n' \leq n} P_{n'} \sigma_{n,n'}, \tag{3.8}$$

$$E_n = -\frac{{Z_n}^2}{2n^2} + \sum_{n' \geq n} P_{n'} \frac{Z_{n'}}{{n'}^2} \sigma_{n',n}, \tag{3.9}$$

total energy of the electronic system becomes

$$< H >= -\sum_n P_n \frac{{Z_n}^2}{2n^2}.$$

The inner shell electrons screens the nuclear charge, so the interaction with the outer shell electrons is included in the energy level. This result is natural in view of the electrostatic interaction and gives the same expression introduced by More[13].

In the central-field approximation, the spin-orbit interaction[24] is

$$\sum_k \xi(r_k) L_k \cdot S_k$$

where L_k is the orbital angular momentum operator and S_k is the spin angular momentum of the kth electron. The function $\xi(r)$ is given by

$$\xi(r) = \frac{1}{2m^2c^2} \frac{1}{r} \frac{dV}{dr}$$

in a central-field potential $V(r)$. m and c are the mass of electron and the speed of light. Since we use Schiff's notations, units are not atomic but cgs-Gaussian.

Using the coulomb potential $V(r) = -Z_k e^2/r$ in the SHM and the classical orbit radius $r_k = a_k n(k)^2/Z_k$, we obtain

$$\xi(r_k) = \frac{c^2}{2me^2 {a_0}^3} \frac{{Z_k}^4}{n(k)^6}$$

where e and a_0 are the elementary charge and the Bohr radius. By comparison with the Eq. (3.7), σ should be proportional to a factor ${Z_k}^3/n^4$. Though the simple Z^3 dependence of the screening constant can be explained as the spin-orbit interaction of the hydrogenic wave function in the Coulomb potential, the coefficient C in Table 3.3 does not decrease so rapidly as n^{-4} when n increases.

3.2.5 Summary

Energy level data recommendation by the screening constant of the screened hydrogenic model is proposed. For high-Z ions, the screening constant is more useful and more accurate than the quantum defect for energy level data recommendation. While the quantum defect converges to a small value near zero as Z increases, the screening constant monotonously decreases. Furthermore, the screening constant has clear Z dependence as Z^3 for $Z = 10 \sim 40$, as $Z^{3.5}$ for $Z = 40 \sim 70$, and as Z^4 for $Z > 70$. Using the simple Z dependence, we have made a fitting formula for He-like ions. By the fitting formula, the energy level of ground state for all He-like ions can be calculated with errors of a few % for He, less than 0.2 % for $Z > 10$, and less than 0.1 % for $Z > 20$. For excited levels, errors are much smaller. The same Z dependence of the screening constant was found for different ions, Li-like, Be-like, and etc. We have seen discontinuous Z dependence of the screening constant in Kelly's data for B-like, C-like, N-like, O-like, and F-like ground state ions. The error in energy level due to the discontinuity is estimated to be about 0.7 % for the ground state of Be-like ion of $Z = 29$ if the simple Z^3 dependence is adopted. Though this simple Z^3 dependence of the screening constant can be explained as the spin-orbit interaction of the hydrogenic wave function in the Coulomb potential, the coefficient in the fitting formula does not decrease so rapidly as n^{-4} as also predicted by the spin-orbit interaction when n increases.

3.3 Occupation probability in the "chemical picture"

3.3.1 Introduction

Calculating spectra of opacity and emissivity is one of the most important subjects in atomic process study of plasmas. In calculating them, we usually have to make an appropriate model for analysis. But we always meet a difficult: how many excited states we have to take into account. In the Schrödinger equation of the Coulomb potential, there are infinite number of eigenvalues near ionization limit. If a certain plasma effect, i.e. cutting off the highly excited states is neglected, the number of states diverges and atomic level population cannot be calculated. This is known as divergence of the atomic internal partition function and has been discussed for a long time[25]. This problem is schematically shown in Fig. 3.13.

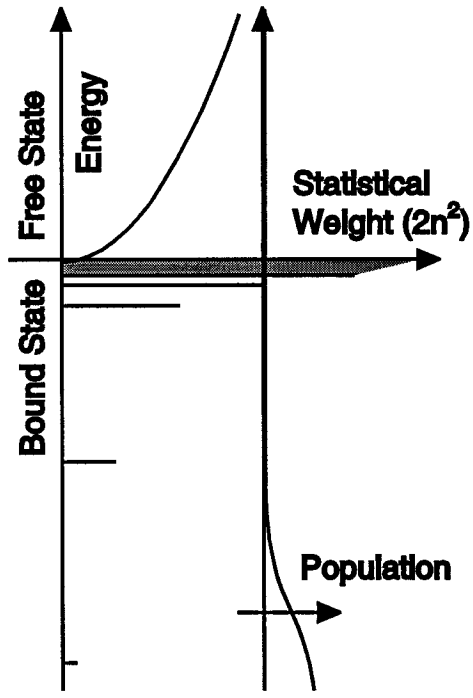

Figure 3.13: Schematic figure of the statistical weight and the population of atomic system in a plasma. There is infinite number of eigenvalues near ionization limit if we neglect a plasma effect.

Roughly speaking, two models are proposed: one is a model which solves the detailed interaction between charged particles like the Planck-Larkin partition function (physical picture)[26] and the other is a model which does not discuss the details of the interaction but the energy and the statistical weight before and after reaction (chemical picture)[27]. In this section, we report a new analytical expression of the occupation probability of highly excited states in the "chemical picture" using the Holtsmark field and saddle-point estimates.

3.3.2 Formulation

We follow a basic formulation of occupation probability by Hummer[25]. The Boltzmann law for atomic level populations says that the population N_i of state i with energy E_i relative to the ground state of an atom in thermal equilibrium at temperature T is

$$N_i \propto g_i \exp\left(-\frac{E_i}{kT}\right) \tag{3.10}$$

where g_i is the statistical weight of the state i. The total number of atoms of the species in question is then proportional to the so-called internal partition function

$$Z_{\rm int} = \sum_i g_i \exp\left(-\frac{E_i}{kT}\right). \tag{3.11}$$

As the sum over all bound atomic states includes those near the ionization limit for which $E_i \to$ const., $Z_{\rm int}(T)$ diverges.

The approach that we have exploited is known as the occupation probability method, in which an occupation probability w_i is inserted into the Boltzmann law and the partition function. Thus we rewrite Eqs. 3.10 and 3.11 as

$$N_i = w_i g_i \exp\left(-\frac{E_i}{kT}\right) \Big/ \tilde{Z}_{\rm int}(T) \tag{3.12}$$

and

$$\tilde{Z}_{\rm int}(T) = \sum_i w_i g_i \exp\left(-\frac{E_i}{kT}\right). \tag{3.13}$$

We can interpret w_i as the probability of finding the atom in state i relative to similar ensembles of non-interacting particles or as the factor by which interactions with the plasma reduce the phase space available to the atomic state in equation. If $w_i \to 0$ sufficiently rapidly as $i \to \infty$, the internal partition function $\tilde{Z}_{\rm int}(T)$ is finite.

The basic idea of the Stark ionization picture is that a bound state i can exist only if the field strength F is smaller than some critical value F_i^c, which depends on the state i. The probability that the bound state i exists is then

$$w_i = \int_0^{F_i^c} dF\, P(F), \tag{3.14}$$

where $P(F)$ is the microfield distribution function. In this section, we try to find a simple expression of w_i using the saddle-point estimates for F_i^c and the Holtsmark field for $P(F)$.

In the saddle-point estimates of F_i^c, the orbital electron in a hydrogenic ion was assumed to move in the sum of the Coulomb potential arising from the nuclear charge Z_a and the potential $\boldsymbol{F}\cdot\boldsymbol{r}$, where $\boldsymbol{F}$ is the magnitude of the microfield assumed to be spatially uniform and independent of time. This composite potential has a saddle point, as illustrated in Fig. 3.14. The assumption is that no bound states exist above the saddle point. For a state of ionization potential E_n, the critical field is then easily shown to be

$$F^c(E_n) = \frac{{E_n}^2}{4Z_a}. \tag{3.15}$$

In the following, we use atomic units. For a hydrogenic ion we have

$$E_n = \frac{{Z_a}^2}{2n^2}, \tag{3.16}$$

$$F_n^c = \frac{{Z_a}^3}{16n^4}. \tag{3.17}$$

n is the principal quantum number of the state.

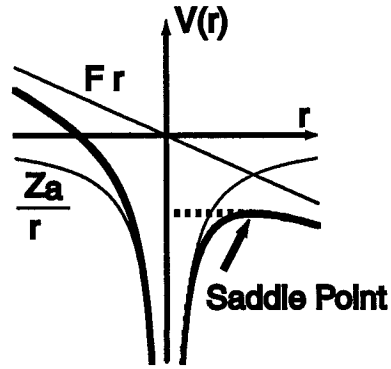

Figure 3.14: Schematic figure of the saddle point of hydrogenic ions in uniform electric field.

The probability of finding the field vector $\boldsymbol{F}$ in $\boldsymbol{F}, \boldsymbol{F}+d\boldsymbol{F}$ is in general

$$W_0(\boldsymbol{F}) = \int\cdots\int \delta\left(\boldsymbol{F} - \sum_{j=1}^{n} \boldsymbol{F}_j\right) p(\boldsymbol{r}_1, \boldsymbol{r}_2, \cdots, \boldsymbol{r}_n)\, d\boldsymbol{r}_1 d\boldsymbol{r}_2 \cdots d\boldsymbol{r}_n \tag{3.18}$$

where the Coulomb field produced by the jth particle is

$$\boldsymbol{F}_j = -Z_p \boldsymbol{r}_j / {r_j}^3. \tag{3.19}$$

Z_p is perturber charge[28]. p is the probability of having particle 1 in $\boldsymbol{r}_1, \boldsymbol{r}_1 + d\boldsymbol{r}_1$, etc. If the charged particles are evenly distributed, Eq. 3.18 can be reduced to be the Holtsmark field,

$$H(\beta) = F_0 W(F) = \frac{2}{\pi}\beta \int x \exp[-x^{3/2}] \sin(\beta x)\, dx \tag{3.20}$$

where $\beta = F/F_0$,

$$F_0 = 2\pi Z_p \left(\frac{4N_p}{15}\right)^{2/3}, \tag{3.21}$$

and N_p is the number density of the perturber ion. In Fig. 3.15, we show the Holtsmark field for reference.

We are now discussing highly excited states. If the saddle-point estimates are a good approximation, such highly excited states rapidly decrease even in the presence of weak electric field. All we have to take into account is then $\beta \sim 0$ part of the Holtsmark field. If $\beta \sim 0$, we know simple relation $\sin(\beta x) \sim \beta x$. Using the relation, we can analytically integrate the equation of the Holtsmark field as

$$H(\beta) = \frac{4\beta^2}{3\pi}. \tag{3.22}$$

Actually, we can see the parabolic shape near $\beta \sim 0$ in Fig. 3.15.

Using the saddle-point estimates, we have

$$w_n = \int_0^{F_n^c} dF\, P(F) = \frac{5^2 {Z_a}^8}{2^{17}\pi^4 n^{12} {Z_p}^3 {N_p}^2}. \tag{3.23}$$

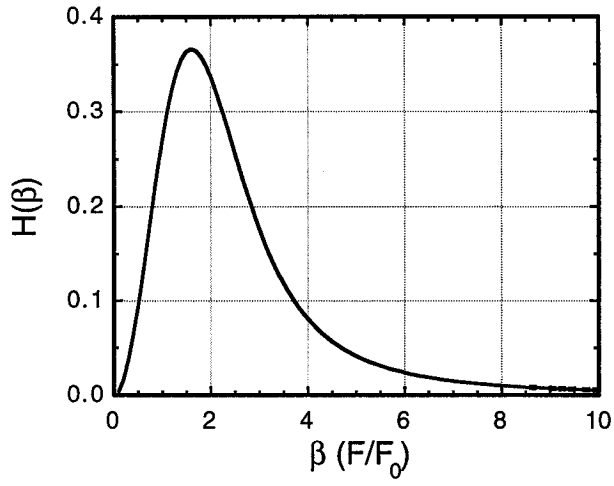

Figure 3.15: Holtsmark field. We can see the parabolic shape near $\beta \sim 0$.

This expression is so simple that we can estimate the occupation probability by the nuclear charge and the principal quantum number of the ion, and the nuclear charge and the number density of the perturber ion. In detail, the occupation probability is proportional to the 8th power of the nuclear charge and inverse proportional to the 12th power of the principal quantum number of the ion. And it is inversely proportional to the nuclear charge cubed and the number density squared of the perturber ion. Equation (3.23) can be more than unity for small n. In the case, we have to adopt unity instead of the given value by Eq. (3.23).

Fortunately we can appeal to theoretical calculation to support our result. Hummer showed the numerical results of the occupation probability for H and He^+ plasmas presented in Figure 3 in Ref. [29]. We can see simple n^{-12} dependence of the occupation probability. In Table 3.4 are displayed the occupation probabilities for two models for hydrogenic carbon. In this case, microfield stems from the mixture of C^{6+} and C^{5+}. Equation (3.23) is changed to be

$$w_n = \int_0^{F_n^c} dF\, P(F) = \frac{5^2 {Z_a}^8}{2^{17}\pi^4 n^{12}({Z_p}^{3/2}N_p + {Z_p'}^{3/2}N_p')^2}, \tag{3.24}$$

where Z_p' and N_p' is the nuclear charge and the number density of another ion. The first model in Table 3.4 is given by Eq. (3.14) using the Holtsmark field exactly[30]. The second is the result by Eq. (3.24). We can see that Eq. (3.24) roughly gives the critical principal quantum number where bound states disappear. Due to the quadratic approximation for the Holtsmark field, numerical values of the occupation probability near the critical principal quantum number are at most three times larger than those estimated with the exact one. For highly excited states, Eq. (3.24) gives almost exact values.

Of course, there should be a certain limitation of this simple expression for the occupation probability since we used the Holtsmark field and the saddle-point estimates in the chemical picture. However, this simple expression of the occupation probability gives basic reference numerical values for quantitative comparison study with the result by a detailed model in which the ion-ion correlation is taken into account or the quantum mechanical calculation has been done.

Table 3.4: Comparison of occupation probabilities at $T_e = 1 \times 10^6$ and $\rho = 1 \times 10^{-2}$g/cm^3 for hydrogenic carbon.

n	Holtsmark	This Model
1	1.00	1
2	9.97(−1)	1
3	9.50(−1)	1
4	4.90(−1)	1.68(−1)
5	5.25(−2)	1.16(−2)
6	4.63(−3)	1.30(−3)
7	5.19(−4)	2.04(−4)
8	7.79(−5)	4.11(−5)
9	3.19(−6)	2.82(−6)

3.3.3 Summary

We propose a simple analytical expression for the occupation probability of highly excited states in low-density hydrogenic plasmas. This expression is based on the "chemical picture" and is derived by using the Holtsmark field and the saddle-point estimates. We believe that this expression would be a basic model in the chemical picture since ion-ion correlation is neglected and the simple saddle-point estimates are used. If density of the plasma is low enough and the temperature is high enough, this expression would be a good approximation. If not, this model roughly gives the critical principal quantum number where bound states disappear and basic reference numerical values of the occupation probability for quantitative comparison study with numerical results by detailed modeling.

References

[1] P. T. Springer, D. J. Fields, B. G. Wilson, J. K. Nash, W. H. Goldstein, C. A. Iglesias, F. J. Rogers, J. K. Swenson, M. H. Chen, A. Bar-Shalom, and R. E. Stewart, Phys. Rev. Lett. **69**, 3735 (1992).

[2] B. Yaakobi, D. Steel, E. Thorsos, A. Hauer, and B. Perry, Phys. Rev. Lett. **39**, 1526 (1977).

[3] B. A. Hammel, C. J. Keane, T. R. Dittrich, D. R. Kania, J. D. Kilkenny, R. W. Lee, and W. K. Levedahl, J. Quant. Spectrosc. Radiat. Transfer **51**, 113 (1994).

[4] H. Griem, 1974, *Spectral Line Broadening by plasmas* (New York: Academic Press).

[5] 山本学, 村山精一, プラズマの分光計測, (学会出版センター, 東京, 1990).

[6] R. W. Lee, *User Manual for RATION*, (Lawrence Livermore National Laboratory, 1990).

[7] For example, I. P. Grant, B. J. McKenzie, P. H. Norrington, D. F. Mayers, and N. C. Pyper, Comp. Phys. Commun. **21**, 207 (1980).

[8] R. L. Kelly, J. Phys. Chem. Ref. Data. **16**, Supplement 1 (1987).

[9] M. J. Seaton, *The Opacity Project* (Institute of Physics Publishing, Bristol and Philadelphia, 1995).

[10] M. J. Seaton, *The Opacity Project* (Institute of Physics Publishing, Bristol and Philadelphia, 1995), p. 173.

[11] J. C. Slater, Phys. Rev. **36**, 57 (1930).

[12] H. Mayer, Los Alamos Scientific Laboratory Report LA-647, 1947.

[13] R. M. More, J. Quant. Spectrosc. Radiat. Transfer **27**, 345 (1982).

[14] R. Marchand and S. Caillé, and Y. T. Lee, J. Quant. Spectrosc. Radiat. Transfer **43**, 149 (1990).

[15] F. Perrot, Phys. Scripta **39**, 332 1989.

[16] W. A. Lokke, and W. H. Grasberger, Lawrence Livermore National Laboratory Report No. UCRL-52276 (1977).

[17] T. Nishikawa, and H. Takabe, Laser and Particle Beams **11**, 81 (1993).

[18] J. Sugar, J. Phys. Chem. Ref. Data. **14** Supplement 2 (1985).

[19] W. C. Martin and R. Zalubas, J. Phys. Chem. Ref. Data **8**, 817 (1979); *ibid.*. **12**, 323 (1983); *ibid.*. **14**, 751 (1985).

[20] Y. Accad, C. L. Pekeris, and B. Schiff, Phys. Rev. A **4**, 516 (1971).

[21] D. R. Plante, W. R. Johnson, and J. Sapirstein, Phys. Rev. A **49**, 3519 (1994).

[22] L. I. Schiff, *Quantum Mechanics 3rd ed.*, (McGRAW-HILL, New York, 1968), p. 255.

[23] D. R. Bates, A. E. Kingston, and R. W. P. McWhirter, Proc. R. Soc. London, Ser. A **267**, 297 (1962).

[24] L. I. Schiff, *Quantum Mechanics 3rd ed.*, (McGRAW-HILL, New York, 1968), p. 433.

[25] D. G. Hummer, and D. Mihalas, 1988, Astrophys. J., **331**, 794.

[26] F. J. Rogers, 1986, Astrophys. J., 310, 726.

[27] W. Däppen, L. Anderson, and D. Mihalas, 1987, Astrophys. J., **319**, 195.

[28] H. Griem, 1974, *Spectral Line Broadening by plasmas* (New York: Academic Press), p. 17.

[29] D. G. Hummer, 1995, in *The Opacity Project*, ed. M. J. Seaton (Bristol and Philadelphia: Institute of Physics Publishing), p. 173.

[30] C. A. Iglesias, and F. J. Rogers, 1995, Astrophys. J., **433**, 460.

Chapter 4

Conclusions

We have developed a general opacity code "CORONA". The code can calculate opacity and emissivity used in the hydrodynamic code of laser plasma simulations.

As the atomic model, the azimuthal quantum number l has been taken into account in the electron energy levels. Based on the statistical model, we have given a solution for the difficulty we meet whenever we use the average ion model; the line profile modeling. Using the opacity and emissivity, we were able to reproduce the corresponding experimental results from laser produced high-Z plasmas, especially, spectra from the plasmas.

For highly ionized plasmas, we have shown a new method for the electron energy level data recommendation. In the method, the screening constant of the screened hydrogenic model is used as the index. We have also shown a simple expression of cutting-off the highly excited states. These method and model will help us to make an appropriate model of highly ionized plasmas.

We summarize the results of the different chapters in the followings as conclusions.

Chapter 1

We have summarized atomic models that have been used in the hydrodynamic codes of the inertial confinement fusion research, i.e., the screened hydrogenic model (SHM), the detail of the rate coefficients, the model for the pressure ionization and the continuum lowering, the collisional radiative equilibrium (CRE) model and the local thermodynamic equilibrium (LTE) model, and the detail of formulae of the emissivity and opacity calculations.

In Sec. 2.3, we have shown a new model for calculating the spectral opacity and emissivity of high-Z plasma like gold for solving the X-ray transport in hydrodynamic codes. In the model, plasmas are assumed in the CRE. The l-splitting effect, i.e., the consideration of the azimuthal quantum number in the electron energy levels is introduced using the SHM developed by Perrot. As a result of a gold plasma, the electron energy level E_4 of Au^{+40}, for example, splits into four sublevels with the width of about 300 eV by including the l-splitting effect. The transitions between the sublevels, such as $4d-4f$, are important elements to understand the strong peak near 200 eV in the experimental spectra of gold plasmas.

In Sec. 2.4, we have shown a line profile modeling for the average ion model. For the opacity and emissivity of the partially ionized high-Z plasmas like gold, the line profile is approximated to be the Gaussian profile of which width is determined by the ionic distribution of different charge states. This opacity and emissivity are installed into the

hydrodynamic code ILESTA-1D to examine the experimental spectra. As a result of the simulation, the peaked X-ray near 200 eV seen in the experiment stems from the lines due to the $\Delta n = 0$ transition between the sublevels of $n = 4$. In addition, relatively flat spectra in $h\nu = 400 \sim 800$ eV seen in the experiment can be explained as a result of the l-splitting of the line of the $4 - 5$ transition. The line group of the $4f - 5g$, $4d - 5f$, and $4p - 5d$ transitions mainly forms this flat structure.

In the simulation of the X-ray generation by laser produced plasmas like gold, the assumptions that the plasmas are in the CRE, the l-splitting effect, and the line profile modeling if the average ion model is used, are essentially important to reproduce the global structure of the X-ray spectrum of the corresponding experiment.

In Sec. 2.5, we have examined the accuracy of this atomic model for the opacity and emissivity calculation of the high-Z plasmas in detail.

We have compared the values of the electron energy level and oscillator strength with the values by the Hartree-Fock-Slater (HFS) model. From the HFS results, as a number of electrons in the level of $n = 4$ increases, the oscillator strength of $n = 4 - 5$ decreases, while the oscillator strength between sublevels of $n = 4$ increases. Errors in the oscillator strength used in Sec. 2.3 are estimated at most about a factor of 2 to those of the level of $n = 4$.

We have discussed the j-splitting effect briefly. For the high-Z ions like gold, the transition energy of the $4d - 4f$ obtained by the SHM with l-splitting does not differ substantially from the detailed theoretical value including the spin orbit interaction. The transition energy of the $4p - 4d$, however, split into two line group, i.e., at about 33 Å for $4p_{1/2} - 4d$ and at about 50 Å for $4p_{3/2} - 4d$. The line group of the lower energy corresponds to transition given by the SHM, but the line group of which energy is higher than that of $4d - 4f$ is purely j-splitting effect. The two-splitted structure of the soft X-ray region is actually observed in the experiment of the Pb. Inclusion of the j-splitting effect would be a next subject in future.

We have shown the accuracy of the population for each charge state that is calculated from the fractional population of the average ion model by the comparison with those obtained by the detailed configuration accounting (DCA) model on the aluminum plasmas. In the DCA model, the rate equation for each charge state is solved separately. Although it also shows a small shift of the distribution of the charge state to the lower temperature side, the distribution can be well reproduced even in the case of low-Z plasma.

Finally, we have shown the comparison study between the spectral opacity based on the model developed in this chapter and the results by detailed opacity codes for the case of hydrogen, carbon, and iron plasmas.

For the low density and low discharged hydrogen plasma, it is difficult to estimate the correct average ionization degrees with the average ion model.

In the case of the carbon plasma more than the solid density, the continuum state near ionization threshold is almost occupied by free electrons. This treatment for the free states can be easily installed into the average ion model. But there are no reliable experimental results of such extreme condition that can be compared with the theoretical results.

From the density dependence of the mean opacity of iron plasmas, we have obtained the applicable density limit of the present model. In the case of low density less than 0.01g/cm^3, the contribution of the term-splitting becomes important. As it seldom occurs that the plasmas of such density becomes important in the usual laser produced plasma, we can conclude the opacity data by the CORONA is good enough for the simulation of

the laser produced plasmas.

For the energy level related to the L shell ($n = 3$), the SHM can give accurate values which can be compared with the experimental ones, while for the energy level related to the M shell ($n = 3$), the SHM can not give accurate values enough. Determining the energy level related to the M shell is also difficult for other detailed opacity codes, since the effect of the spin-orbit interaction becomes important.

Chapter 2

Energy level data recommendation by the screening constant of the screened hydrogenic model is proposed. For high-Z ions, the screening constant is more useful and more accurate than the quantum defect for energy level data recommendation. While the quantum defect converges to a small value near zero as Z increases, the screening constant monotonously decreases. Furthermore, the screening constant has clear Z dependence as Z^3 for $Z = 10 \sim 40$, as $Z^{3.5}$ for $Z = 40 \sim 70$, and as Z^4 for $Z > 70$. Using the simple Z dependence, we have made a fitting formula for He-like ions. By the fitting formula, the energy level of ground state for all He-like ions can be calculated with errors of a few % for He, less than 0.2 % for $Z > 10$, and less than 0.1 % for $Z > 20$. For excited levels, errors are much smaller. The same Z dependence of the screening constant was found for different ions, Li-like, Be-like, and etc. We have seen discontinuous Z dependence of the screening constant in Kelly's data for B-like, C-like, N-like, O-like, and F-like ground state ions. The error in energy level due to the discontinuity is estimated to be about 0.7 % for the ground state of Be-like ion of $Z = 29$ if the simple Z^3 dependence is adopted. Though this simple Z^3 dependence of the screening constant can be explained as the spin-orbit interaction of the hydrogenic wave function in the Coulomb potential, the coefficient in the fitting formula does not decrease so rapidly as n^{-4} as also predicted by the spin-orbit interaction when n increases.

We propose a simple analytical expression for the occupation probability of highly excited states in low-density hydrogenic plasmas. This expression is based on the "chemical picture" and is derived by using the Holtsmark field and the saddle-point estimates. We believe that this expression would be a basic model in the chemical picture since ion-ion correlation is neglected and the simple saddle-point estimates are used. If density of the plasma is low enough and the temperature is high enough, this expression would be a good approximation. If not, this model roughly gives the critical principal quantum number where bound states disappear and basic reference numerical values of the occupation probability for quantitative comparison study with numerical results by detailed modeling.

謝辞

ずいぶん長くかかりましたが、あきらめもせず見守っていただいた三間圀興教授の存在なくしては、本論文は決してまとめることが出来なかったと思います。終始懇篤なるご指導、ご鞭撻を賜りましたこと共々、深厚なる感謝の意を表します。

第2章は、著者が大阪大学大学院工学研究科に在学中より始めた研究をまとめたものです。在学中、ご指導、ご教示頂いた、高部英明教授、西原功修教授、加藤義章教授(現、原研関西研光量子センター長)、中井貞雄教授、西村博明助教授に深く感謝します。特に、高部教授には、手ほどきから研究の仕方をご教授いただきました。

また、方位量子数 l をエネルギー準位に入れる重要性、内部量子数 j を考慮したエネルギー準位のデータ提供など、この章の重要な結論を得る際に、有益な示唆を頂いたヘブライ大学 M. Finkenthal 教授にも深く感謝します。

さらに、バグだらけのオパシティーコードを受け入れて、コード間比較研究の仲間に入れた頂いたオパシティーワークショップの参加者、諮問委員会の方々にも深く感謝します。このワークショップへの参加なしには、現状ほどオパシティー計算、プラズマ中原子過程のモデリングへの深い理解はあり得ませんでしたし、こだわりも生まれませんでした。

第3章において、有益な助言をいただいた Lawrence Livermore National Laboratory (LLNL) の Richard M. More 博士（現、核融合研教授）に深く感謝します。第2章の内容は More 博士が LLNL にいらっしゃったときに執筆された教科書を元にしていることを含めて、プラズマ中原子過程研究の世界の水準を教えて頂きました。

岡山大学赴任後、著者の勝手、気ままな研究を許していただいた、古谷洋一郎名誉教授、福山淳教授（現、京都大学教授）に深く感謝します。また、この論文をまとめることを最優先させていただいた奈良重俊教授にも厚く感謝します。

最後に、この研究を大阪大学大学院在学中より援助して頂いた両親、この論文をまとめるにあたって協力してくれた家族にも感謝します。

業績目録

主要論文

1. "X-ray emission and transport in gold plasmas generated by 351-nm laser irradiation", H. Nishimura, H. Takabe, K. Kondo, T. Endo, H. Shiraga, K. Sugimoto, T. Nishikawa, Y. Kato, S. Nakai, Physical Review A Vol. 43, 1991, pp. 3073-3085.

2. "統計手法を用いた高Zプラズマの原子モデル", 西川亘、中村真嗣、高部英明、三間圀興, 核融合研究 68 別冊, 145 (1992).

3. "Line profile modeling for non-LTE partially ionized plasmas based on average atom model with l-splitting", T. Nishikawa, H. Takabe and K. Mima, Laser and Particle Beams Vol. 11, 1993, pp. 81-87.

4. "Non-LTE atomic modeling for laser-produced plasmas", H. Takabe, S. Nakamura and T. Nishikawa, Laser and Particle Beams Vol. 11, 1993, pp. 119-126.

5. "Soft x-ray spectra of highly ionized elements with atomic numbers ranging from 57 to 82 produced by compact lasers", G. M. Zeng, H. Daido, T. Nishikawa, H. Takabe, S. Nakayama, H. Aritome, K. Murai, Y. Kato, M. Nakatsuka, and S. Nakai, Journal of Applied Physics Vol. 75, 1994, pp. 1923-1930.

6. "Computational model for non-LTE atomic process in laser produced plasmas", H. Takabe, and T. Nishikawa, Journal of Quantitative Spectroscopy and Radiative Transfer Vol. 51, 1994, pp. 379-395.

7. "Improved Screened Hydrogenic Model", T. Nishikawa, 12th International Conference on Laser Interaction and Related Plasma Phenomena Osaka, Japan, April 24-28, 1995. (AIP CONFERENCE PROCEEDINGS 369, pp. 422-427)

8. "Energy level data recommendation by screening constant", T. Nishikawa, to be published in Journal of Quantitative Spectroscopy and Radiative Transfer.

9. "Simple Expression of Occupation Probability in the 'Chemical Picture' ", T. Nishikawa, to be published in the April 10 2000 issue of The Astrophysical Journal Vol. 533.

発表論文

1. "Ion Kinetic Effect on Fusion Reaction Rate", T. Nishikawa, H. Takabe and K. Mima, Japanese Journal of Applied Physics Vol. 28, 1989, pp. 2004-2010.

国際会議発表

1. "Computational Model for Non-LTE Atomic Process in Laser Produced Plasmas", H. Takabe, and T. Nishikawa, Proceeding of the 5th international conference on Radiative properties of hot dense matter 1992.

2. "Plasma x-ray source of various materials produced by compact solid state lasers", G. Zeng, H. Daido, S. Nakayama, K. Murai, T. Nishikawa, S. Kiyokawa, H. Takabe, H. Aritome, M. Nakatsuka, Y. Kato, S. Nakai, SPIE Technical Conference on "Application of Laser Plasma Radiation", 14-16 July 1993, SPIE Proceeding Vol. 2015.

3. "Population Inversion in Recombining Li-like Al Plasma", T. Nishikawa, and K. Nishihara, The 9th APS Topical Conference on Atomic Processes in Plasmas, San Antonio, Texas, USA, September 19-23, 1993.

4. "Improved Screened Hydrogenic Model", T. Nishikawa, 12th International Conference on Laser Interaction and Related Plasma Phenomena, Osaka, Japan, April 24-28, 1995.

本論文と関係する紀要

1. "Opacity Code "CORONA"", T. Nishikawa, and H. Takabe, WorkOP-III:94, Garching, Germany, 7-11 March 1994.
("WorkOp-III:94 Final Report", edited by A. Rickert, K. Eidmann and J. Meyer-ter-Vehn, F. J. D. Serduke, and C. A. Iglesias, MPQ 204, Max-Planck-Institut für Quantenoptik, 1995.)

2. "Recommended Atomic Data for Collisional-Radiative Model of Li-like Ions and Gain Calculation for Li-like Al Ions in the Recombining Plasmas", T. Nishikawa, T. Kawachi, K. Nishihara, and T. Fujimoto, Research Report, National Institute of Fusion Science, NIFS-DATA-30 (1995).

3. "Opacity Code "CORONA"", T. Nishikawa, WorkOP-IV:97, Madrid, Spain, 26-30 May 1997. Final Report in press.

本論文に関連する国内学会発表

1. "X線輻射輸送における l-splitting の効果", 西川亘, 高部英明, 三間圀興, 日本物理学会, 講演番号 1pTF7, 1990.4.1, 大阪大学.

2. "高Zプラズマ中でのX線輻射輸送－ l-splitting effect and line profile modeling －", 西川亘, 高部英明, 三間圀興, 日本物理学会, 講演番号 3aT8, 1990.10.3, 岐阜大学.

3. "高Zプラズマ中でのX線輻射輸送－ l-splitting を含んだ原子過程－", 西川亘, 高部英明, 三間圀興, 日本物理学会, 講演番号 25pD7, 1991.3.25, 学習院大学.

4. "輻射駆動爆縮におけるアブレーション構造の解析", 西川亘, 高部英明, 三間圀興, 日本物理学会, 講演番号 30pG6, 1991.9.3, 北海道大学.

5. “急激な温度、密度変化を伴うプラズマ中での非平衡輻射輸送”, 西川亘, 高部英明, 三間圀興, 日本物理学会, 講演番号 30pZA7, 1992.3.30, 慶応大学.

6. “レーザー生成高Zプラズマからの X 線スペクトルのシミュレーション”, 西川亘, 村井健介, 高部英明, 三間圀興, 加藤義章, M. Finkenthal, 日本物理学会, 講演番号 27aZK14, 1992.9.27, 東京大学.

7. “再結合プラズマ中での反転分布形成シミュレーションにおける原子過程モデル依存性－リチウム様アルミニウムの場合－”, 西川亘, 西原功修, 日本物理学会, 講演番号 15aDA1, 1993.10.15, 岡山大学.

8. “再結合プラズマ中での反転分布形成シミュレーションにおける原子過程モデル依存性 II”, 西川亘, 西原功修, 日本物理学会, 講演番号 30pE5, 1994.3.30, 福岡工業大学.

9. “オパシティー計算のための遮蔽水素モデル”, 西川亘, 日本物理学会, 講演番号 2aL11, 1994.9.2, 静岡大学.

10. “遮蔽水素モデルを用いた He-like イオンのエネルギー準位”, 西川亘, 日本物理学会, 講演番号 27aYA6, 1995.9.27, 大阪府立大学.

11. “混成原子モデルを用いた高Zプラズマの l －分布を含んだポピュレーションの計算”, 西川亘, 日本物理学会, 講演番号 30aR1, 1995.9.30, 大阪府立大学.

12. “X 線分光スペクトルとプラズマの温度・密度の関係”, 西川亘, 日本物理学会, 講演番号 31aYG-5, 1997.3.31, 名城大学天白キャンパス.

13. “水素プラズマ分光スペクトルの理論計算”, 西川亘, 電気学会プラズマ研究会, 講演番号 EP-97-27, 1997.5.16, 岡山大学.
（電気学会プラズマ研究会資料 EP-97-27, 7-10 頁）

14. “水素プラズマにおける 1 次の摂動波動関数を考慮したシュタルク効果の理論計算”, 西川亘, 日本物理学会, 講演番号 7pYN-4, 1997.10.7, 神戸大学六甲台地区.

15. “1 次の摂動波動関数を考慮した L β 線スペクトルプロファイルの厳密計算”, 西川亘, 日本物理学会, 講演番号 31p-YR-9, 1998.3.31, 東邦大学, 日本大学.

16. “プラズマ中マイクロフィールドによるシュタルク効果を用いた高励起状態の状態数の計算”, 西川亘, 日本物理学会, 講演番号 28a-L-12, 1998.9.28, 琉球大学、沖縄国際大学.

17. “シュタルク効果に基づく高励起状態数の計算”, 西川亘, 日本物理学会, 講演番号 25a-B-1, 1999.9.25, 岩手大学.

その他国内学会発表

1. “爆縮プラズマ中での核反応にイオンの運動論的効果”, 西川亘, 高部英明, 三間圀興, 日本物理学会, 講演番号 5aK5, 1989.10.5, 鹿児島大学.